CRYSTALLITE FORMATION WITHIN LM105 BULK METALLIC GLASS VIA CONTROLLED HEAT TREATMENT CYCLING WITH CONSIDERATIONS FOR OPTIMAL CRUCIBLE MATERIAL AT HIGH TEMPERATURES

BY

KATHRYN RUSSELL

A THESIS
SUBMITTED TO THE FACULTY OF

ALFRED UNIVERSITY

IN PARTIAL FULFILLMENT OF THE REQUIREMENTS
FOR THE DEGREE OF

MASTER OF SCIENCE

IN

GLASS SCIENCE AND ENGINEERING

ALFRED, NEW YORK

FEBRUARY, 2017

CRYSTALLITE FORMATION WITHIN LM105 BULK METALLIC GLASS VIA CONTROLLED HEAT TREATMENT CYCLING WITH CONSIDERATIONS FOR OPTIMAL CRUCIBLE MATERIAL AT HIGH TEMPERATURES

BY

KATHRYN RUSSELL

B.S. ALFRED UNIVERSITY (2014)

SIGNATURE OF AUTHOR signature on file

APPROVED BY signature on file

ALEXIS CLARE, ADVISOR

signature on file

HERBERT GIESCHE, ADVISORY COMMITTEE

signature on file

WILLIAM LACOURSE, ADVISORY COMMITTEE

signature on file

CHAIR, ORAL THESIS DEFENSE

ACCEPTED BY signature on file

ALASTAIR M CORMACK, DEAN
KAZUO INAMORI SCHOOL OF ENGINEERING

ACKNOWLEDGMENTS

Foremost, I would like to express my appreciation for the continuous support, encouragement, and guidance provided by my thesis advisor, Dr. Alexis Clare.

I would also like to thank the rest of my thesis committee: Dr. Herbert Giesche and Dr. Bill LaCourse for their invaluable input and ongoing support via thoughtful comments, questions, and materials.

This project would not have advanced without the support of Stephanie O'Keefe and Glenton Jelbert of LiquidMetal Technologies in Rancho Santa Margarita, CA, and their generous donation of LM105 samples.

Furthermore, I offer my sincerest thanks to the lab support provided by Francis Williams, Anatoly Kishinevski, Ryan Dempsey, Yiyu Li, Diksha Kini, and Yin Liu. This project would not have moved forward without their help.

Last but not least, I would like to thank my family and friends, particularly my mother and father, Susan and Robert Griffith, my boyfriend, Daniel Bourlotos, and my homie Diksha Kini for always encouraging me to push forward and never give in.

TABLE OF CONTENTS

LIST OF TABLES

LIST OF FIGURES

ABSTRACT

Crystallites consisting of Zr, Ti, Cu, and Ni were formed within an amorphous matrix by reheating samples of the glassy metal LM105 to 405°C. The absence of Al in the crystallite formation suggests that this aluminum remained within the amorphous matrix. The sequence of crystallite formation was investigated using standard x-ray diffraction of samples heated to 5 different temperatures in 20°C steps from 365 to 405°C, and for times from 0 to 60 minutes. The glass transition temperature, measured via differential scanning calorimetry in argon atmosphere, was verified to be between 385°C and 405°C using Archimedes density measurements. The optimal material for interfacing with the molten LM105 alloy was also investigated via a superheated interaction study. In this study, samples of polished, fully amorphous, LM105 were placed on alumina, zircon, silicon nitride, silicon carbide, and Syalon 050, 101, 110, and 201 substrates. These were heated to 1250°C at 5°C per minute in a 95/5 Ar-H atmosphere. The samples were then analyzed using a FEI Co., Inc., Quanta 200F environmental SEM with an EDAX Genesis system. Substrate cross sections revealed that zircon underwent the least corrosion in contact with superheated LM105, implying, that out of the substrates tested, this is most robust for high temperature applications where ceramics interface directly with molten LM105. This includes initial glass forming techniques such as counter-gravity casting.

INTRODUCTION

Due to the state of the ever changing, technology driven, societies we live in, new advancements in materials have emerged. Metallic glasses are a product of these advancements with their unique combination of metal alloys with amorphous structures and their altered physical, chemical, and electrical properties. These properties present advantages for a number of applications. Bulk metallic glasses, which can be processed using methods similar to those used by inorganic glasses, find use in industrial coatings, defense applications, electronics casings, fine jewelry, medical devices, sporting goods, space projects, and hinge applications in the mobile phone industry1. Characteristic properties of most metallic glasses include: high yield strength, high hardness, superior strength to weight ratio, superior elastic limit, high corrosion resistance, high wear-resistance, and unique acoustic properties1.

Metallic glasses were first discovered in 1960 by Pol Duwez and his colleagues at California Institute of Technology[1] via the rapid solidification processes (RSP). RPS produces metals with a glassy structure by cooling from a molten state at rapid cooling rates, around $10^5 Ks^{-1}$. In order to achieve these high cooling rates, the specimens needed to be thin, along the lines of 20-50μm. As a result of this requirement, the specimens created were generally foil, wire, or powder. Combining the fact that these alloys would crystallize after a period of 24 hours at room temperature and their small size, their use for industrial or consumer applications was very limited[1].

After the first discovery of metallic glasses via RSP, investigators began work in two distinct systems, metal-metals and metal-metalloids. Metal-metal systems include only non-metalloid constituents while metal-metalloid systems contain both metals and metalloids (though the metalloids generally only constitute 20% of the total composition)[2]. The following study was undertaken with the intent of studying only metal-metal alloy systems or commercial viability. The original metallic glass alloys were composed of only two components, Ag (75at.%) and Si (25at.%). After the discovery of their instability, further research into more stable alloys was conducted.

The first advancements in the creation of bulk metallic glasses (BMGs), which are inherently more stable as demonstrated by their slower cooling rates and could be created in a larger, more useful size, began with the work of Chen in 1974[2]. Chen was able to create BMG rods of Pt and Pb by water cooling methods which are much slower than RSP[2]. This brought about the first questions on what constitutes a bulk metallic glass. According to Suryanarayana and Inoue, the conditions for consideration of an amorphous metal as a bulk metallic glass are: (1) the alloy must have a thickness greater than 1mm (2) the alloy must have at least three components, (3) the alloy must have a critical cooling rate, R_c, no higher than $10^3 Ks^{-1}$ (thus promoting stability), and (4) the alloy must exhibit a large supercooled liquid region[1].

The original compositions developed by Chen and team contained hazardous materials, thus limiting their industrial or commercial application. Through further research the best modern candidate fitting the BMG requirements is called Vitreloy1, and is composed of Zr, Ti, Cu, Ni, and Be system[3]. However, due to the toxicity of beryllium, studies continued seeking to replace Be with a less hazardous, suitable replacement. Through extensive research, it was found that a suitable replacement for Be in Vitreloy1 would be Al[4]. LiquidMetal Technologies in Santa Maragrita, CA has successfully created one such commercially viable alloy, described hereto forth as LM105. LM105 is comprised of Zr, Ti, Cu, Ni, and Al. Due to its forming capabilities, low toxicity, high elastic modulus, high strength, and generally pleasing appearance, LM105 became a prime candidate for consumer use. The first products created from this material were focused on sporting equipment, including golf club faces, and baseball bats. Further use of LM105 in industry relies on the ability of the glass to be formed in hollow shapes for use in containers, such as flasks.

The primary method for the creation of hollow shape objects, made with LM105, is counter gravity casting, as described in Patent # US 20140083646 A1[5]. The hollow parts are created by "feeding a molten metal alloy in a counter-gravity direction into a mold cavity to deposit the molten metal alloy on a surface of the mold cavity and then solidifying the deposited molten metal alloy"[5]. During this process the molten metal, as

well as the cooled metallic glass are in contact with either another metal or crucible materials. This patent states that impurities and cooling rate affect the formation of crystals within the glass. However, for this study, it is assumed that all samples were created using the same heating technique and were unaffected by a molten metal interface.

Figure 1 depicts the apparatus used for counter gravity casting. The molten metal is contained in a feed trough, part 440. From this trough the material travels through a pipe, 450, and into the casting reservoir, 460. The part is then formed by injection of air, into the mold cavity. Due to the purity needs of the final product and the high reaction rate of molten metal with O_2, the atmosphere injected is most likely very low in oxygen. The material used in part 460 is, at this time, unknown, but can be inferred to have a high thermal conductivity or heat capacity in order to assist in the increased cooling rate required for BMG creation, $10^5 Ks^{-1}$.

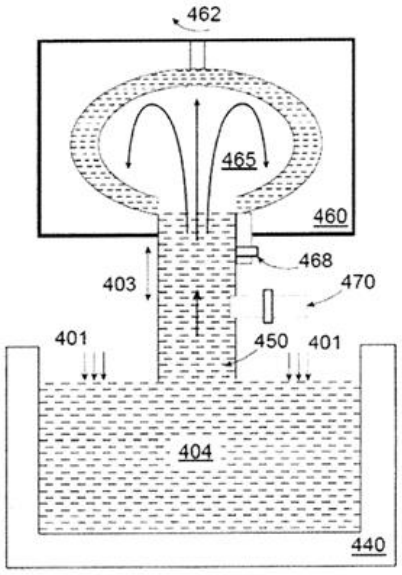

Figure 1. Diagram of counter gravity cast method used for creation of hollow BMG parts5. Parts #440, 460, and pipe materials are of particular interest.

Waniuk et al. believe that small changes in cooling rate have limited effect on the properties, and crystal growth rate. However, the work of Antonysamy et al. shows that varying the temperature at which the material is quenched can affect the localized cooling

rate of the metallic glasses[5]. This does affect the growth of micron or nanometer sized crystallites.[5,6] Antonysamy studied simple $Cu_{47.5}Zr_{47.5}Al_5$ metallic glass rods, with 2mm diameter, which were created with >99.99% pure pre-alloyed ingots. Because these alloys were pre-formed with high purity materials, it is believe that impurities were far less likely and would have no effect on the final crystallite growth rate. The pre-formed ingots were melted in an arc melter with an argon atmosphere and titanium getter, then molded using copper mold suction casting[5]. Through this study it was noted that crystallites formed at the ends and outer edges of the 10-14μm rods. This preferential formation of the crystallites is most likely due to the varied cooling rate at the edges of the copper tubes. This team was able to use x-ray diffraction and physical property measurements to distinguish between fully amorphous and partially crystallized metallic glasses. Figure 2 depicts $Cu_{47.6}Zr_{47.5}Al_5$ x-ray diffraction patterns for fully amorphous and partially crystallized samples. Mechanical analysis of the samples (Figure 3), shows that the CuZr B2 crystallites had an effect on the max yield strength, and stress strain curves of the CuZrAl glass.

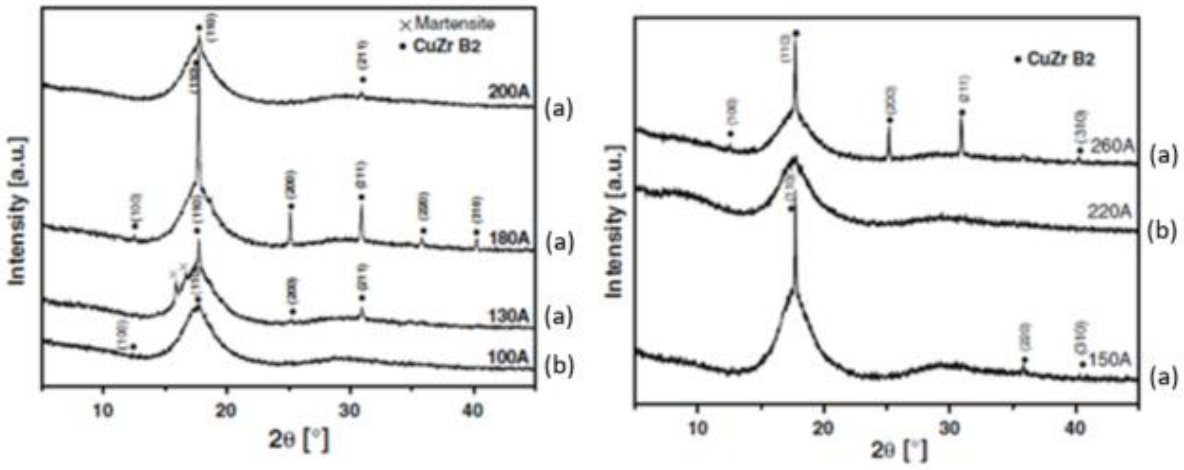

Figure 2. X-ray diffraction pattern of as cast samples of partially crystallized (in (a), 100A; in (b) 200A) and fully amorphous $Cu_{47.6}Zr_{47.5}Al_5$[5] (all other patterns).

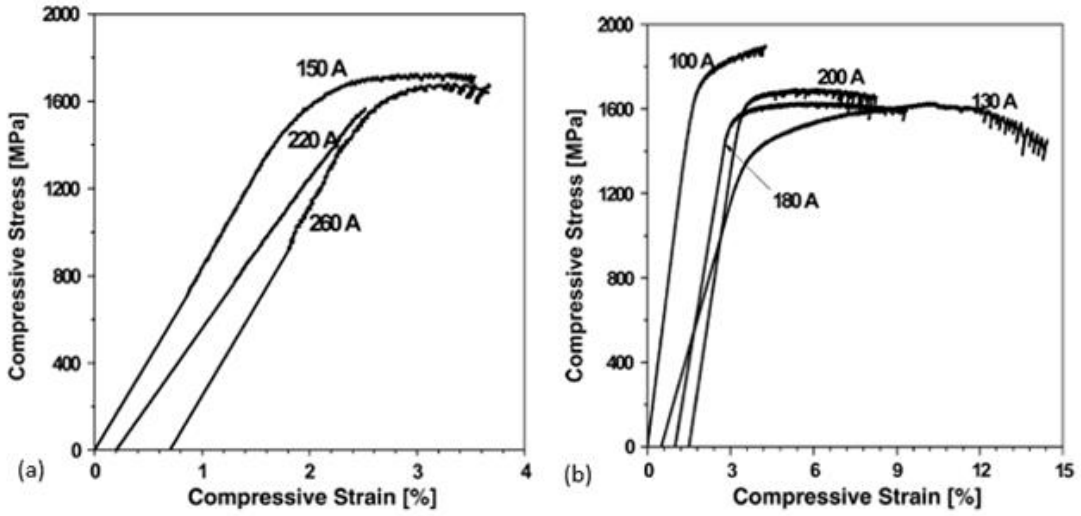

Figure 3. Stress-strain relationship of fully amorphous (in (a), 220A, in (b), 100A) and partially crystallized $Cu_{47.6}Zr_{47.5}Al_5$[5] (all other readings).

There are two main methods for the introduction of crystals in a glassy matrix: (1) devitrification of the glass (2) introduction of reinforcing crystals via the introduction of fibers or particles of a different nature[6]. In order to reduce total cost of commercially available materials, devitrification was pursued as the primary technique. Devitrification can be achieved via two methods: (1) varied cooling rates such as those exhibited via Antonysamy et al.[5], or (2) by controlled heat exposure of fully amorphous metallic glass.

In an effort to pursue technique (1), varied cooling rates, a test was designed for the creation of a BMG using pressed metal powders. Pressed metal powder pellets were created using the compositions listed in Table II. These metals were chosen based on the availability of powdered metals and the wide range of atomic sizes. The variety of atomic sizes helps to create a kinetic barrier to crystal growth during cooling. This is known as the confusion principle. The actual percentage of each metal used was based the works of Dong, et. al., Kuhn, et. al., and Antonysamy, et al[7]. With the help of Justin Kase at Ambrell Induction Heating Solutions, the pellets were melted using an Easy Heat Induction Furnace, Figure 4.

Table I: Pressed Pellet Composition by Weight %.

	I	II	III	IV	V
Zr	51.97	54.98	66.38	64.91	45.99
Ti	6.01	0	0	0	0
Al	10.01	10.02	8.07	10	8.03
Ni	14	5	8.69	10.01	0
Cu	18	30	10.49	15.08	45.99
Nb	0	0	6.38	0	0

The original works referenced had proven that these pellets could be formed into metallic glasses via rapid cooling upon contact with a copper plates[8]. The pellets were melted using induction currents causing an induced magnetic field that forced the sample to hover within the specially wrapped water cooled coils. At the suggestion of the operator, and through some trial and error, these pellets were heated using 500 Amps at 284kHz. This allowed the sample to heat thoroughly and maintain induced levitation. Just prior to stopping the current, liquid nitrogen was poured on and around the copper plate. Once the current was stopped, the samples drop to the nitrogen cooled copper plate, as depicted in Figure 5. The stabilizing bowl, filled with standard ice, was also filled with liquid nitrogen just prior to shutting off the current from the Easy Heat Control Box.

Figure 4. Ambrell Easy Heat Induction Unit[9].

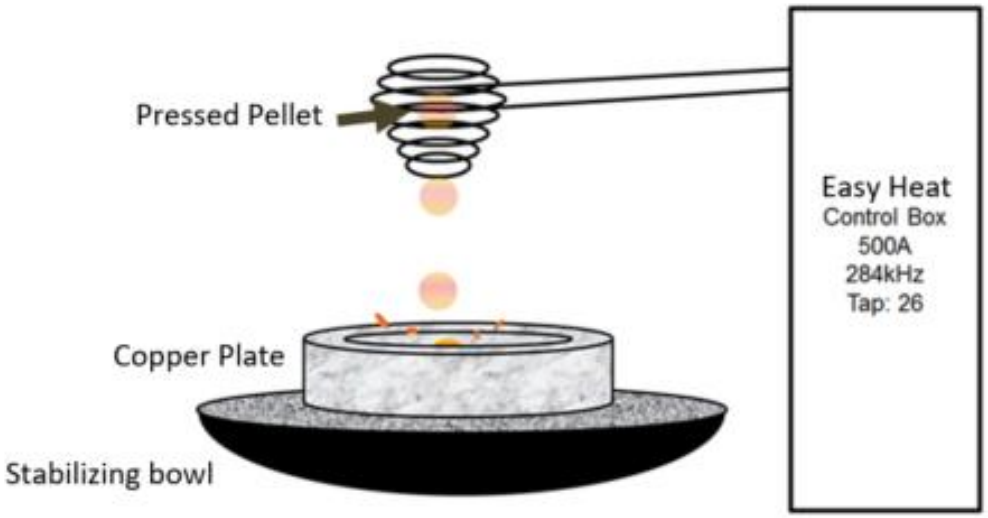

Figure 5. Induction furnace used to melt pressed pellets. Once current from the control box ceased, the sample dropped onto liquid nitrogen cooled copper plate.

For samples I and II, no atmosphere control was used. A dramatic and instantaneous "burning" of the samples was observed. This event took place once the samples were heated to a red hot state. This reaction was best described as super-fast oxidation. In order to prevent this occurrence during additional melting cycles, the best practice would be to perform the melt under vacuum or Argon atmosphere. However, atmosphere control was not available at Ambrell. As a replacement, liquid nitrogen vapor was used to force O_2 away from the sample, Figure 6. Unfortunately the same reaction occurred. It was therefore assumed that the powders used had absorbed high levels of O_2 during storage, pressing, and transport. It is also possible, after examining Ellingham diagrams, such as Figure 7, that the N_2 atmosphere introduced could react violently with the titanium in the system.

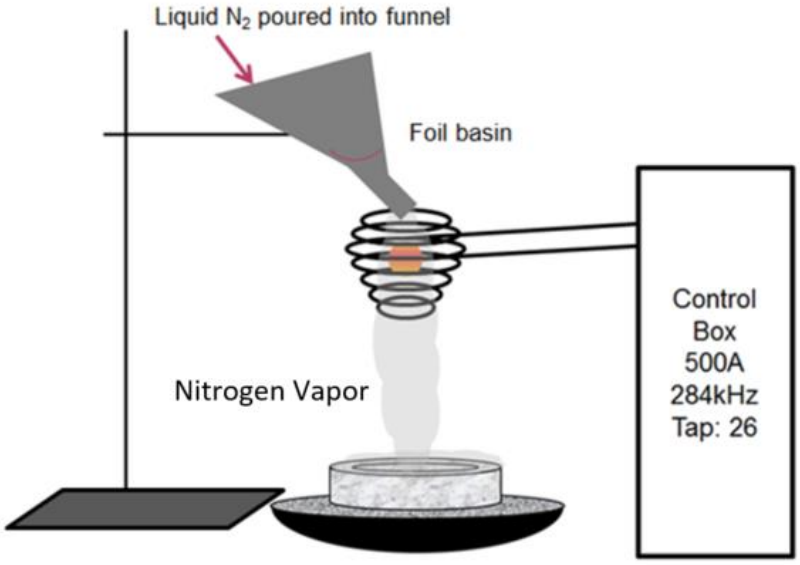

Figure 6. Depiction of additional N_2 atmosphere used to force O_2 away from molten metal during induction heating and rapid cooling.

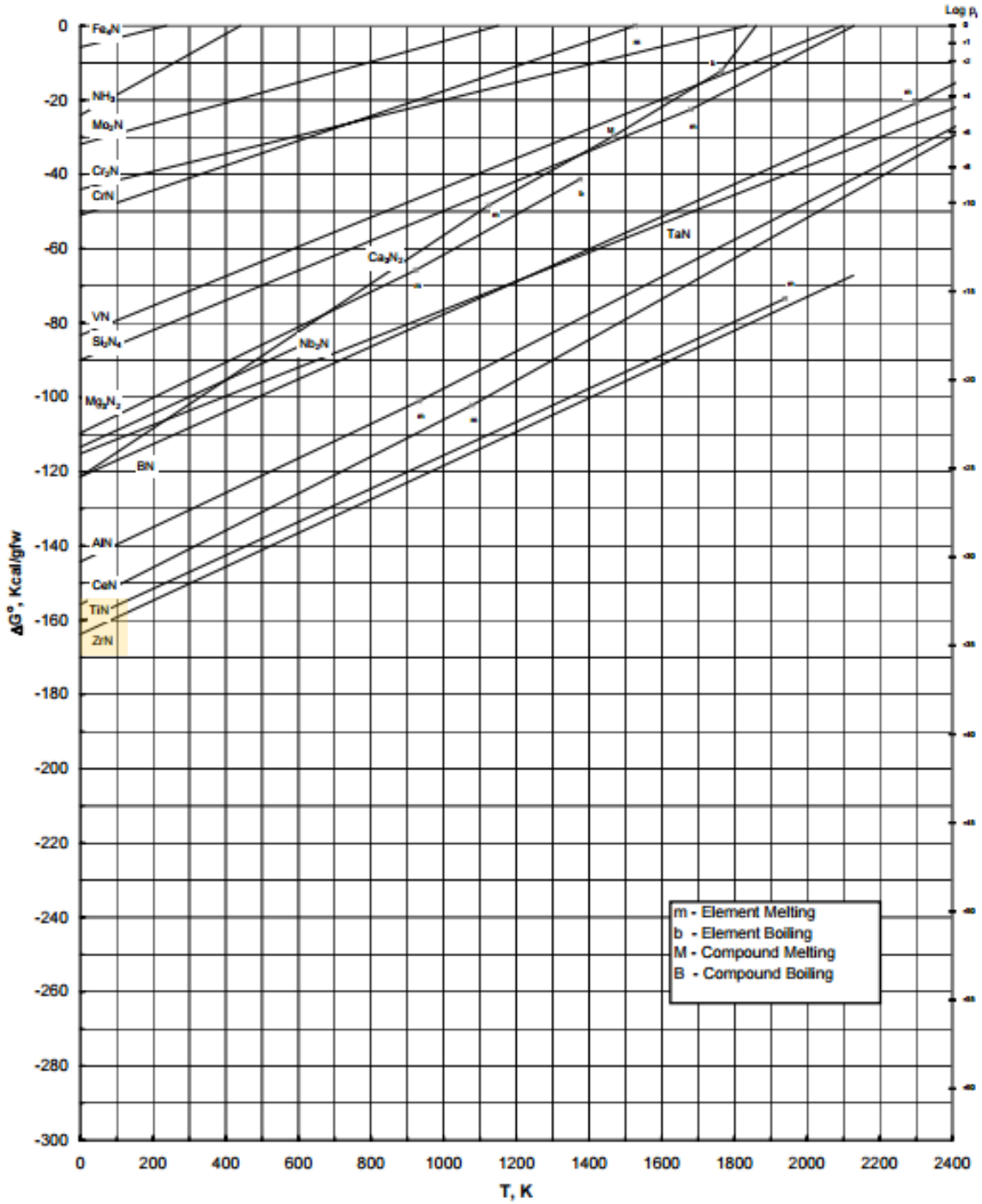

Figure 7. Ellingham diagram showing negative energy (ΔG) requirement for formation of ZrN and TiN.[10]

Commercially available glass is ideal for controlled heat exposure as it is homogeneous and cooled under a controlled rate in order to provide consistent product to customers. Samples of

fully amorphous glass could be used to pursue for crystallite growth via method (2) controlled heat exposure of fully amorphous metallic glass. LM105, created by LiquidMetal, comprised of Zr, Ti, Al, Cu, and Ni (see MSDS in Table II) is ideal for this pursuit as it is high purity and commercially availability.

Table II: LM105 Composition as listed in MSDS.

HAZARDOUS INGREDIENTS	CAS NUMBER	OSHA PEL	ACGIH		% by weight
			TLV	TLV-STEL	
Zirconium	7440-67-7	5mg / m3	10	10	Balance
Titanium (in the form of respirable TiO2)	7440-32-6	5mg /m3	10	N/D	10% max
Copper (in dust form)	7440-50-8	1.0mg / m3	1.0	2.0	20% max
Nickel	7440-02-0	1mg / m3	1.5	10	15% max
Aluminum	7429-90-5	15 mg/m3 (total) 5 mg/m3 (resp)	10 mg/m3	10 mg/m3	5.0% max

Liquid Metal technology compositions are proprietary and covered by many patents, but upon contacting Stephanie O'Keefe of LiquidMetals, a data share agreement was reached and samples of LM105 (an original alloy sample and fully amorphous samples) were attained. The investigation of the crystallization behavior of LM105 was pursued by heat treating the glass at a variety of times and temperatures as outlined in the matrix in the experimental procedure. Along with the BMG samples, LiquidMetals provided differential scanning calorimeter data for LM105. This data shows that the glass transition temperature is ~399°C, while the onset of melting occurs at ~785°C. In order to understand the low temperature crystallization behavior, the time time/temperature matrix for heat treatment was designed around the glass transition. Samples would be heated between 365 and 405°C. The total time needed for full affect at each temperature was unknown, so times were varied from 0 to 60 minutes. The samples heated at these temperatures are hereto forth referred to as "Sample Set 1".

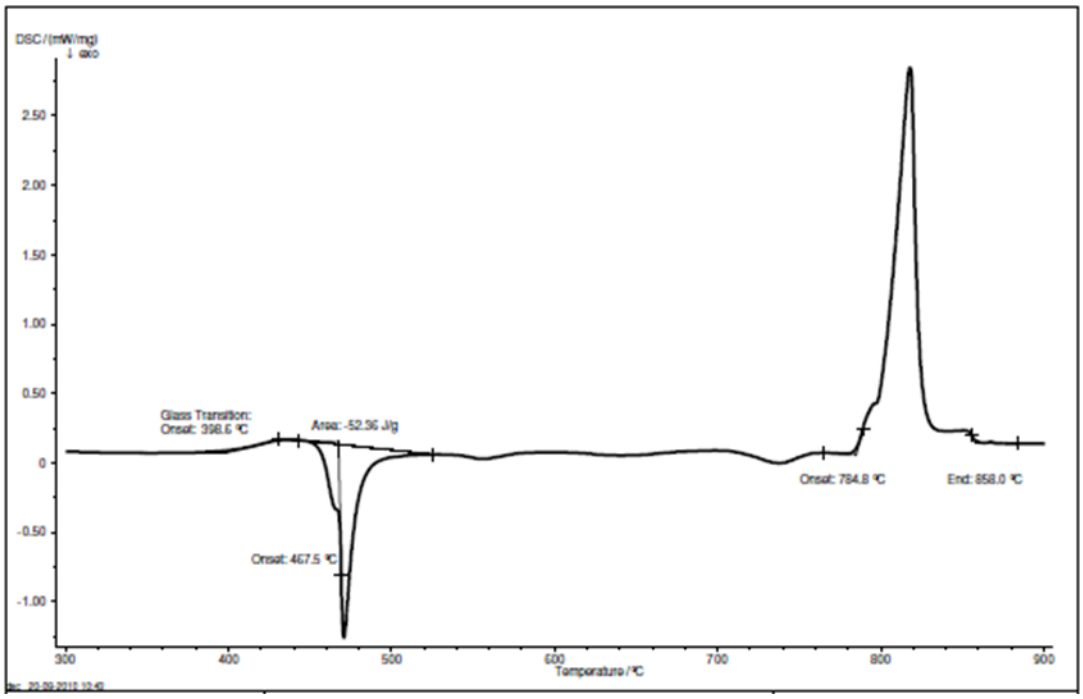

Figure 8. DSC plot for LM105 glass heated in an Ar atmosphere at 5°C/min showing glass transition at ~399°C, and onset of melting at ~785°C.

As part of the data share agreement with alternative crucible materials for the counter gravity casting process were investigated. Many different factors affect the interaction of the ceramic crucible material and molten metal. These include: commercial availability, cost, resistance to corrosion, and maximum use temperature[11]. Substrates were gathered at a variety of costs, availabilities, and max temperature ranges. Zircon and alumina were chosen due to their high commercial availability and low cost. Silicon carbide, and silicon nitride were selected in order to test the effect of non-oxide ceramics on the molten metal, and vice versa. Syalon 101, 110, and 201 were suggested by LiquidMetal due to their status as "advanced ceramic solutions for extreme environments". See Appendix B for more information on material properties.

As wetting angle is a well-known method for understanding the interaction between liquids and solids, the optimal testing method focused on this interaction. Sessile drop testing is often considered the best lab scale method for gaining this type of understanding[12]. Unfortunately, initial attempts at sessile drop testing of LM105 led to oxidation of the metal prior to melting, see Experimental Procedure Section C. An

alternative method for investigation of high temperature interaction is via the investigation of interaction/corrosion depths for materials treated at high temperatures. Generally, this should occur when one material, in this case LM105, is in the molten state. Samples of LM105 were ground and polished to create pristine surfaces for interaction, then heated to ~1250°C, much higher than the onset of melting observed at ~799°C. The samples treated under these conditions were labeled "Sample Set 2."

Using controlled crystallization and improved forming capability, such as that brought about by improved metal-ceramic interaction, it is possible that future metallic glass-crystallite composites could be created. This will enable new technologies through altered physical, chemical, and electrical properties including increased yield strength.

EXPERIMENTAL PROCEDURE

A. Experimental Setup

1. Sample Preparation

5mm x 5mm x 1mm LM105 samples were cut from the bulk amorphous LM105 using a water cooled diamond Dremel cutting wheel. 20mm x 20mm substrate samples of the alumina, zircon, silicon nitride, silicon carbide, and Syalon 050, 101, 110, 200, and XP, were also cut using a water cooled slow saw. BMG samples from Sample Set 1 and Sample Set 2, as well as the substrate to be investigated, were ground and polished to create smooth interaction surfaces. The samples were polished using: 50, 80, 120, 180, 240, 320, 340, 400, 600, 800, 1200, and 1500 grit Silicon Carbide paper followed by a cerium oxide polish. Each of these steps was maintained for 30 seconds, and checked for any visible inconsistencies in the surface texture. If an uneven or scratched surface was observed, polishing continued until no flaws were visible to the eye.

2. Confirming Composition via Energy Dispersive Spectroscopy

As LM105 is highly electrically conductive, these samples were not sputter coated before ESEM analysis. An FEI Co., Inc., Quanta 200F (indicating it is equipped with a field emission gun) with an EDAX Genesis system (EDS) was used to confirm the composition of the LM105 glass prior to heat treatment, Figure 9. The SEM was set to a spot size between 5 and 6, 0.76 Torr atmosphere, 10.60mm working distance, 20kV, and 100s readings time. Each of the 5 measurements was within 0.5wt% deviation of the composition reported in the MSDS, Table II, Table III.

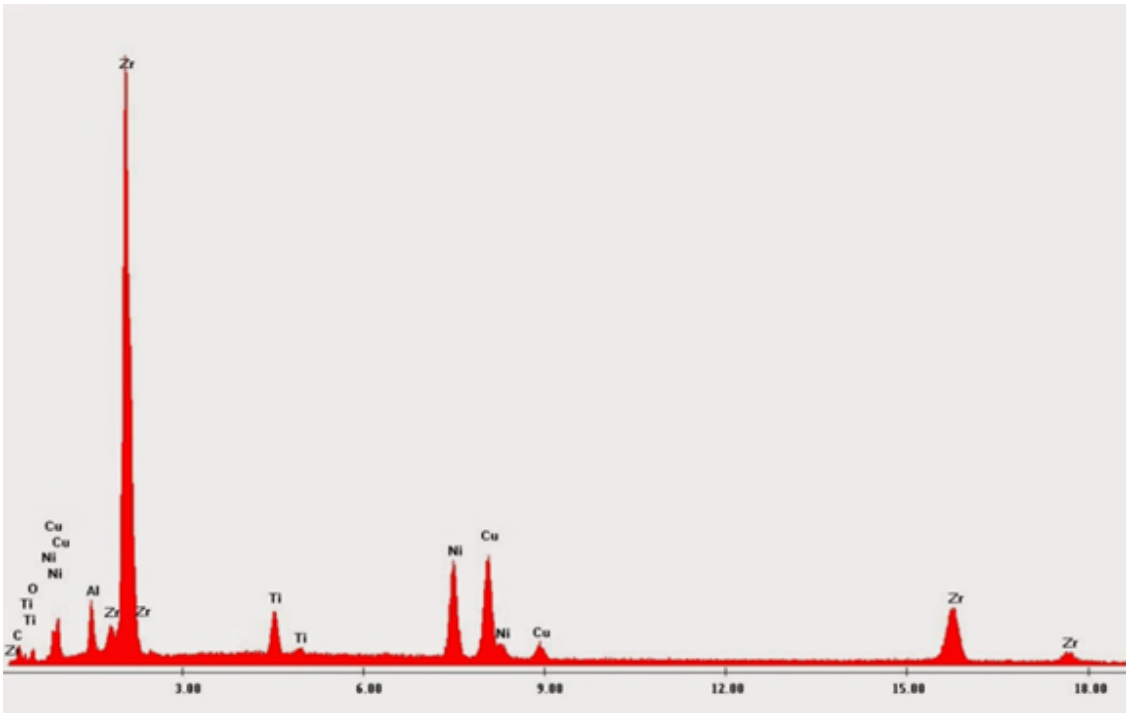

Figure 9. EDS Spectra for crystalline LM105 sample.

Table III: LM105 Composition Measurements Taken via Energy Dispersive Spectroscopy.

LM105	Zr	Cu	Ni	Al	Ti	
1	64.64	15.72	12.74	3.67	3.23	100.0
2	64.43	16.71	12.07	3.67	3.11	100.0
3	64.42	16.25	12.47	3.62	3.32	100.1
4	64.48	16.05	12.6	3.6	3.27	100.0
5	65.96	15.21	11.57	4.19	3.06	100.0
Average	64.79	15.99	12.29	3.75	3.20	100.0
STDEV	0.592	0.504	0.424	0.222	0.098	

B. Low Temperature Heat Treatment of Sample Set 1

Sample Set 1 was used for the investigation of crystallite formation via controlled heat exposure. A Barnstead Thermolyne 21100 tube furnace to be used to heat treat these samples. In this investigation, the prepare LM105 samples were placed on substrates, as listed in Table X. They were then placed in the quartz lining tube with a titanium getter. A 95/5 Argon/Hydrogen atmosphere was pumped through the quartz tube at a rate to induce 5 bubbles per second in bubbler setup in the outgassing tube. This bubble rate was maintained as the samples were heated according to programs in Table IV. The heating

cycle was performed at a rate of 5°C per minute, ascending to and descending from, the desired heat treatment temperatures, with holds from 0 to 60 minutes. This rate was chosen as it is the maximum speed for temperature increase imposed by the furnace capability. The substrates used here included zircon, alumina, silicon carbide, silicon nitride, and graphite. Graphite was added to this study as a test for the effects of carbon on the LM105 samples. Each of the substrates listed was used for a full series of LM105 samples as listed in Table IV. This made for a total of 40 samples in sample set 1.

Table IV: Time and Temperature Matrix for Heat Treatment of Sample Set 1.

Temperature (°C)	Time
385	0
385	15
385	30
385	60
405	30
425	30
445	30
465	30

Once samples returned to room temperature they were carefully removed from the furnace and transferred to sample containers for storage and transfer. The ceramic-metal interface was marked to ensure they could be measured separately. Samples were cleaned with isopropyl alcohol to remove any non-bound species, and mounted on a plastic x-ray diffraction mount using removable putty. They were placed in an XRD D2-phaser in order to obtain x-ray diffraction patterns. The ceramic-metal interface, and the air-metal interface were measured separately. Due to the thickness of the samples, it is believed that the x-ray patterns were not altered by the mounting putty or the plastic mount underneath. As the samples were extremely flat and polished smooth, a longer scan time was used to gather maximum data, Table V. There was no notable difference between the ceramic-metal and air-metal surface x-ray Diffraction patterns.

Table V: X-ray Parameters for Sample Set 1.

Parameter	Value
Start Angle	5°

End Angle	65.017°
# of Steps	1980
Time/step	0.6s
Total Scan Time	0.905556
Spin Rotation	Clockwise

The samples were then cleaned again using isopropyl alcohol and measured for density changes. A standard Archimedes density measurement technique was used to measure the density of each of the metallic glasses. Each sample was weighed three times in air, then submerged in kerosene and measured another three times. The densities were then calculated as shown in equation 1 in which $\boldsymbol{m_{dry}}$ = sample dry weight, $\boldsymbol{m_{wet}}$ = weight when submerged in kerosene, and 0.7776 is the standardized density of kerosene at room temperature. The summary results are listed in table VI.

$$\boldsymbol{\rho = 0.7776 * \frac{m_{dry}}{m_{dry} - m_{wet}}}$$

Table VI: Results of Archimedes Density Measurements.

Treatment Temp (°C)	Treatment Time (Min)	Average (g/cm^3)	StDEV (g/cm^3)
0	0	6.570	0.009
385	0	6.602	0.004
385	15	6.596	0.011
385	30	6.625	0.007
385	60	6.644	0.019
405	30	6.696	0.006
425	30	6.696	0.007
445	30	6.696	0.006
465	30	6.708	0.004

A gauge R&R (reproducibility repeatability test) was run in which 10 samples densities were measured 9 times. Though inherent variability is expected in this type of density measurement, the majority of the variation in sample density was a result of sample to sample variation (part-to-part). This was found using a two-way ANOVA analysis within the Excel SixSigma program. The analysis shows that the vast majority of variation was part-to-part variation, with a small contribution from repeatability (or the

ability to measure the same density when measuring the same part at different times). Figure 10 shows the analysis results. Reproducibility (or the ability to measure the same density between operators) is inherently 0 as only one operator was measuring the densities.

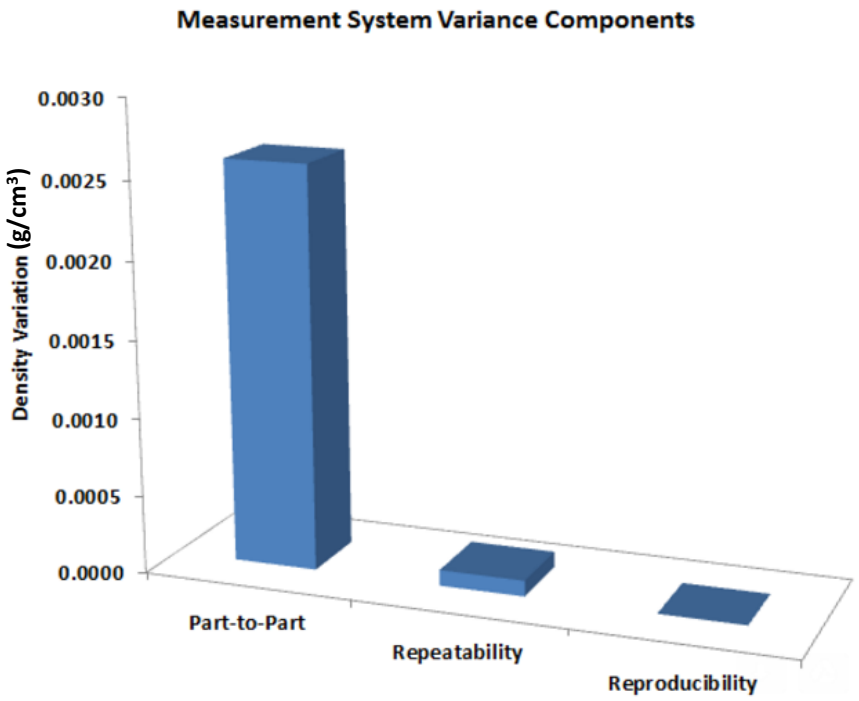

Figure 10. Measurement system variability for 10 sample densities measured 9 times each.

C. High Temperature Heat Treatment of Sample Set 2

A Carbolite 300 series furnace was used to investigate the interaction of the molten LM105 with the substrate materials. These samples are referred to as sample set 2. The Carbolite 300 series furnace was capable of achieving 1500°C, and was modified to meet the inert atmosphere requirements. The furnace provided the capability to heat to 1500°C, but lacked all of the necessary parts. The parts (including the liner tube) were ordered and installed. The alumina tube, supported at both ends by steel ring stands (to prevent sagging during high heat exposure) was inserted into the furnace and windowed end caps were installed and sealed using o-rings and high temperature silicone sealant, Appendix A. After drying, the furnace was tested for air tight capabilities using a positive

pressure soap bubble test. Any leaks were repaired by either resealing or adjustment of the o-rings and end caps. This was repeated between every sample run

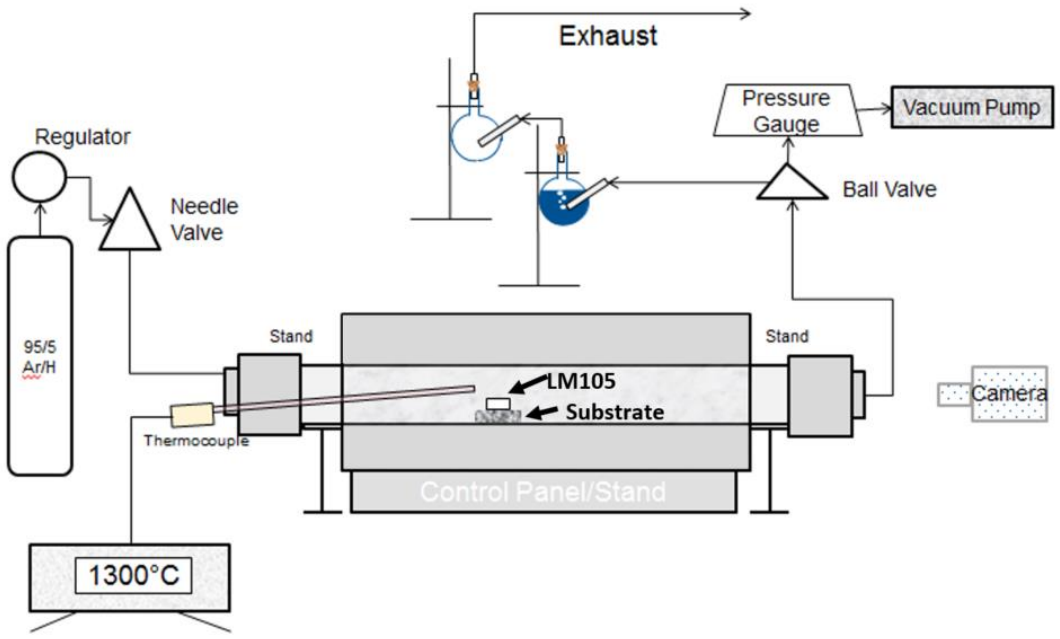

Figure 11. Carbolite tube furnace setup for high temperature heat treatment and sessile drop observation of sample set 2.

Sample Set 2 was run with a similar set of substrates to sample set 1, however Syalon products were added and graphite was removed. The substrates (alumina, zircon, silicon nitride, and Syalons [of International Syalons] 050, 101, 110, and 201) were prepared as per experimental procedure Section A.1.

Each metallic glass sample was placed with its polished side facing the polished substrate surface to ensure proper surface area interface for interaction. The substrate was then placed on a carbon getter to assist in the removal of any oxygen present in the system during heat treatment. The sample and getter were then placed in the furnace and positioned below the thermocouple, as pictured in Figure 11.

In order to remove the atmosphere, a vacuum was pulled on the alumina tube for ~2 minutes. The atmosphere gas, 95%Ar 5%H was then purged through the system for 2 minutes using the vacuum pump. After the vacuum pump was turned off, and the furnace

allowed to fill with gas, the pressure from the gas supply was increased until the bubbling system in Figure 11 reached approximately 3 bubbles per second. Positive pressure was maintained during all testing in order to ensure that any leaks that formed at higher temperatures or over time were accounted for.

For the initial run, the furnace was ramped to a set point of 1300°C for 60 minutes. The actual temperature was recorded every minute for 10 minutes, and the furnace was found to be at 1250±20°C. Visual observation of the samples were made through the heating cycle, but the samples did not appear to melt as expected. Each sample was run through their cycles and carefully removed for analysis.

After removing each sample, digital images of the interaction surfaces were taken, see Appendix C. As the substrates were electrically insulating ceramics, they were then sputter-coated with a thin layer of gold for SEM analysis. The metallic glass sample placed on Syalon 201, silicon nitride, and zircon were destroyed as in Figure 12. Others remained intact, but were not suitable for cross sectional analysis as originally desired. All substrates survived the high temperatures and were suitable for further investigation. The sample surfaces were analyzed using ESEM in low vacuum and in contact with carbon tape in order to minimize surface charging, see results and discussion.

Figure 12. Sample Set 2 examples of destroyed LM105 on associated substrates (left: Zircon and right: Syalon 201).

After initial investigations, see Appendix C, all samples were cleaned using isopropanol and cut perpendicular to the interaction surface using a water cooled slow saw. They were then mounted in epoxy, ground, polished, and coated with a thin layer of

gold coating. Measurements were taken throughout the process to ensure the cross section to be observed was in the center of the interaction area.

RESULTS AND DISCUSSION

A. X-ray Diffraction Results

1. Individual Diffraction Results

Using Jade diffraction pattern analysis program the polished but untreated LM105 x-ray diffraction pattern was analyzed. The samples showed that the glass was highly amorphous, Figure 13.

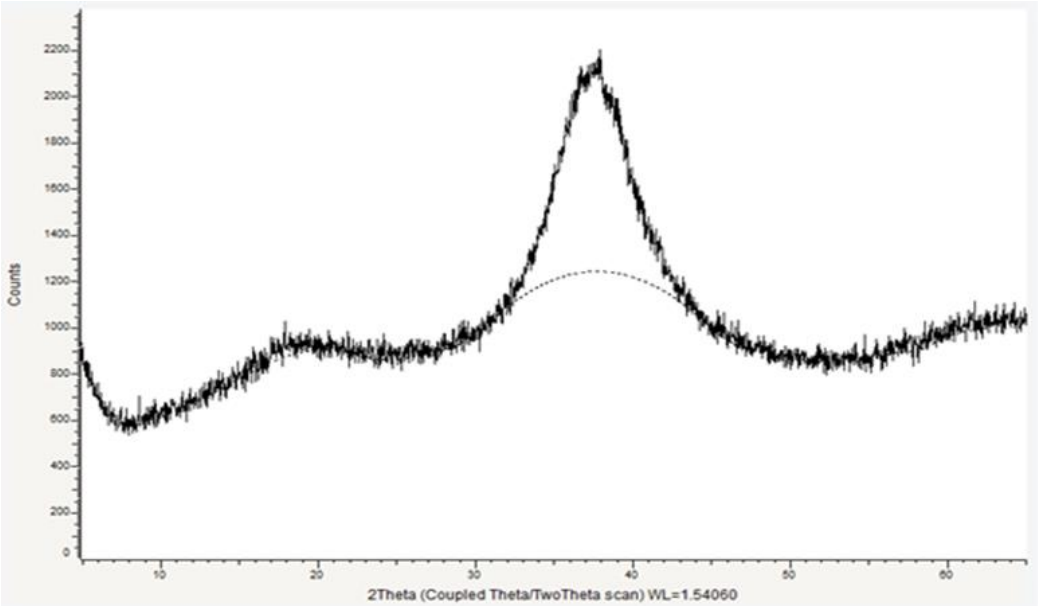

Figure 13. X-ray diffraction pattern of polished, fully amorphous LM105 shows no distinct peaks.

2. Crystallization Sequence

The x-ray diffraction patterns for each sample in sample set were measured, and analyzed for crystalline peaks. These samples showed crystallization of the nickel, titanium, zirconium, and iron. The presence of a large oxide peaks, Figure 14, shows that there was limited success in creating an inert atmosphere, though some can be attributed to the TiO_2 used as a primary component. Figure 17 shows the peaks present after heat treatment at 425°C for 30 minutes. This was used as a bench mark for understanding the crystallization sequencing.

From the x-ray diffraction plots shown below (Figure 14 -Figure 18) the crystallization sequence was recorded. The first peaks to form were indicative of ZrO_2 in the form of Tazheranite, Figure 14. After this phase, a Zirconium, Titanium, Nickel alloy, in the form of $Zr_{1.79}Ti_{0.21}Ni$, formed, Figure 15. Figure 16 shows the addition of CuZr followed by Figure 17, showing a Titanium Nickel, in the form of $Ti_{0.094}Ni_{0.906}$. Lastly, Figure 18 shows high titanium, nickel, zirconium alloy in the form of $Zr_{0.36}$ $Ti_{0.64}Ni$. Ni, Zr, and Ti fall out of solution first (visible in Figure 16). The Aluminum does not appear to be as prevalent in the crystal regions of the patterns suggesting that it remains in the glassy structure. This is similar to results seen by Antonysamy, et al[5]. This may also be attributed to the fact that the Aluminum constitutes only 10wt% of the total glass.

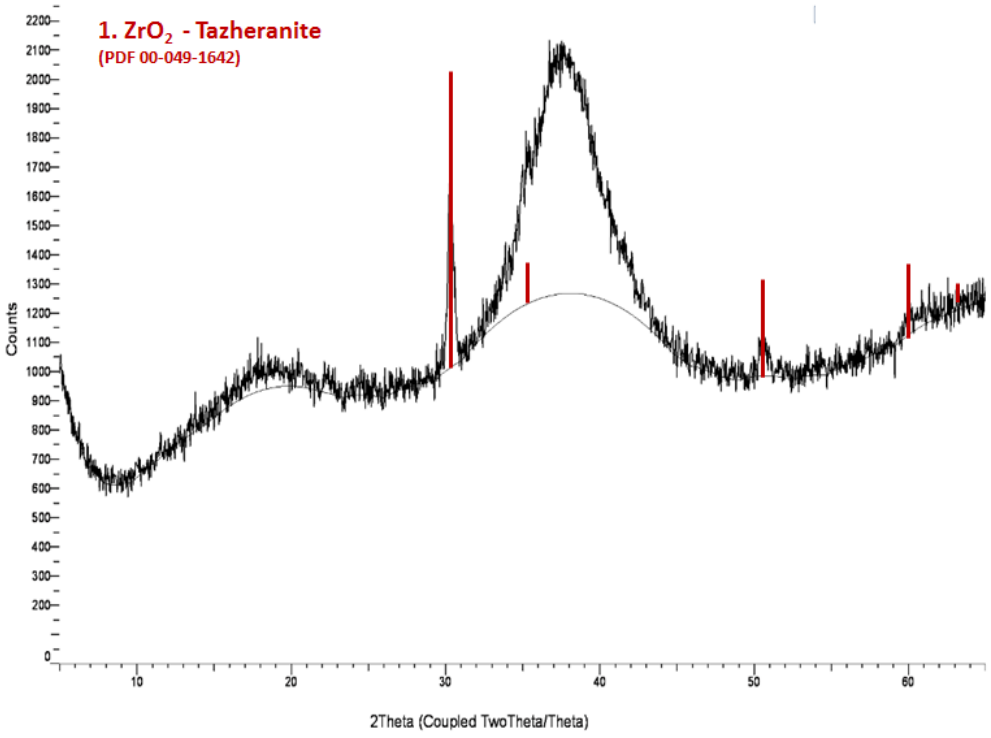

Figure 14. X-ray diffraction pattern of samples treated at 385°C with no hold time. The first peaks formed during crystallization of LM105 are indicative of Taxheranite - ZrO_2.

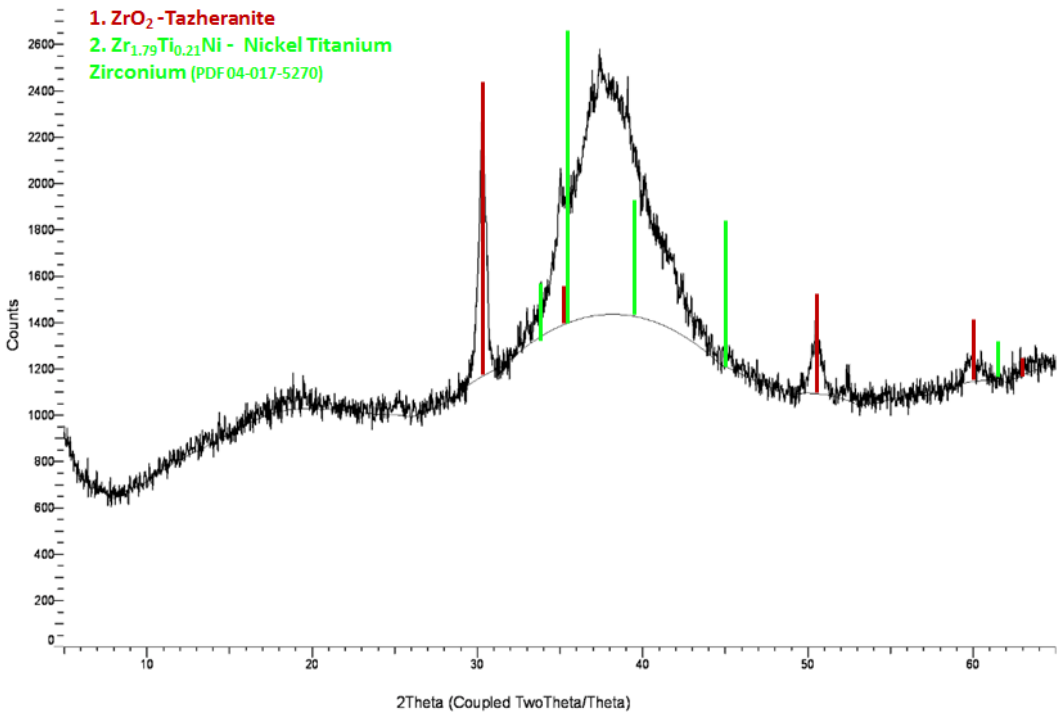

Figure 15. X-ray diffraction pattern of LM105 after heat treatment at 385°C for 60 minutes, showing the additional crystal formation of Zr1.79Ti0.21Ni.

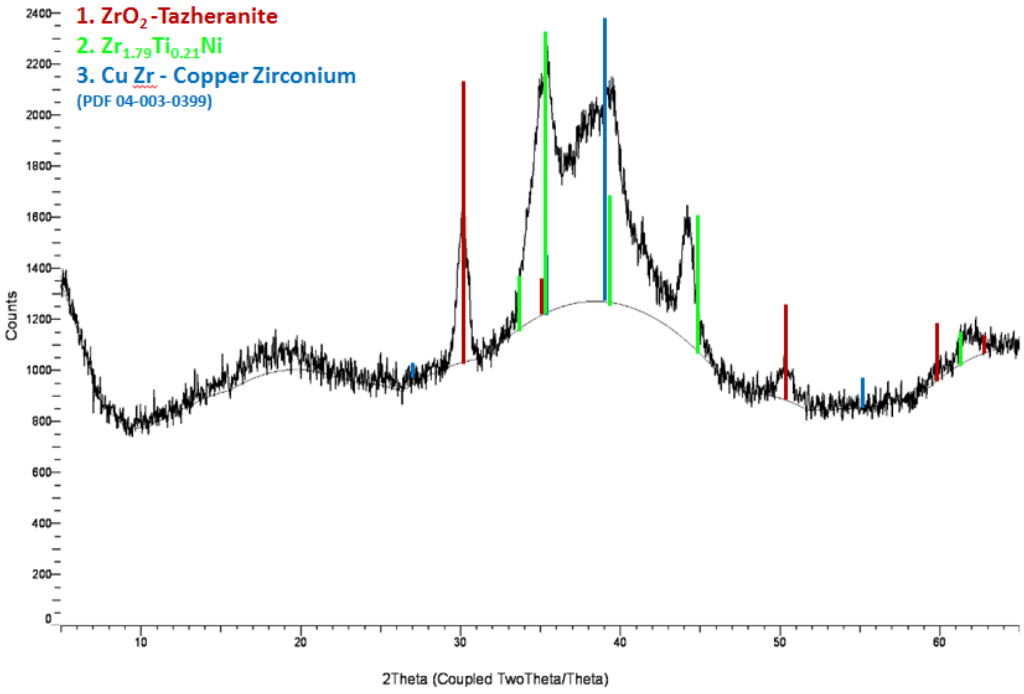

Figure 16. X-ray diffraction pattern of LM105 after heat treatment at 405°C for 30minutes, showing the additional crystal formation of CuZr.

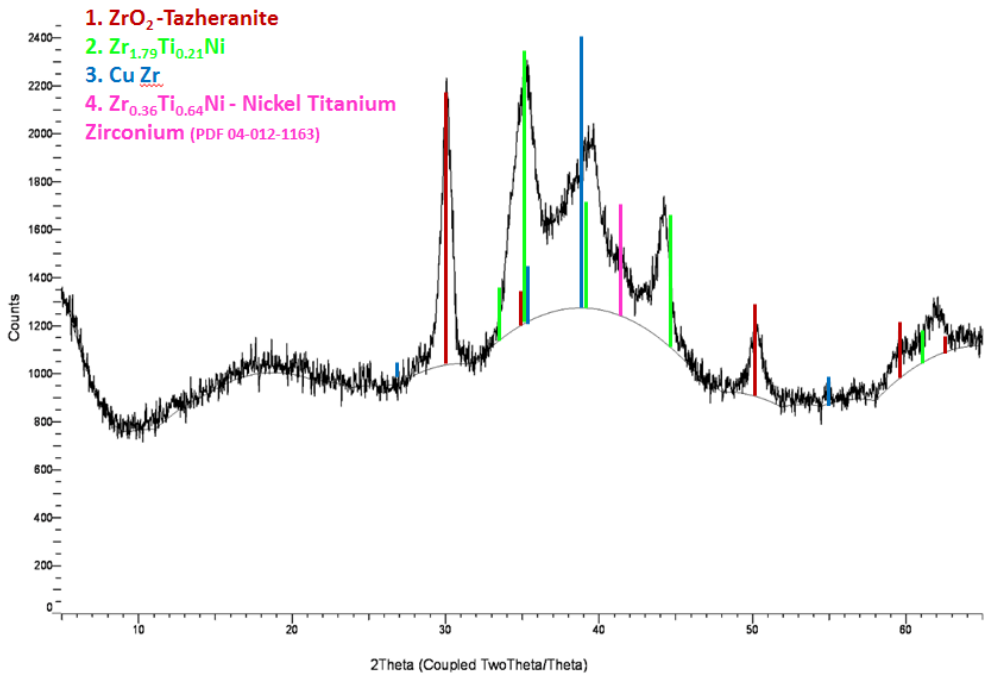

Figure 17. X-ray diffraction pattern of LM105 after heat treatment at 425°C for 30 minutes, showing the additional crystal formation of Zr0.26Ti0.64Ni.

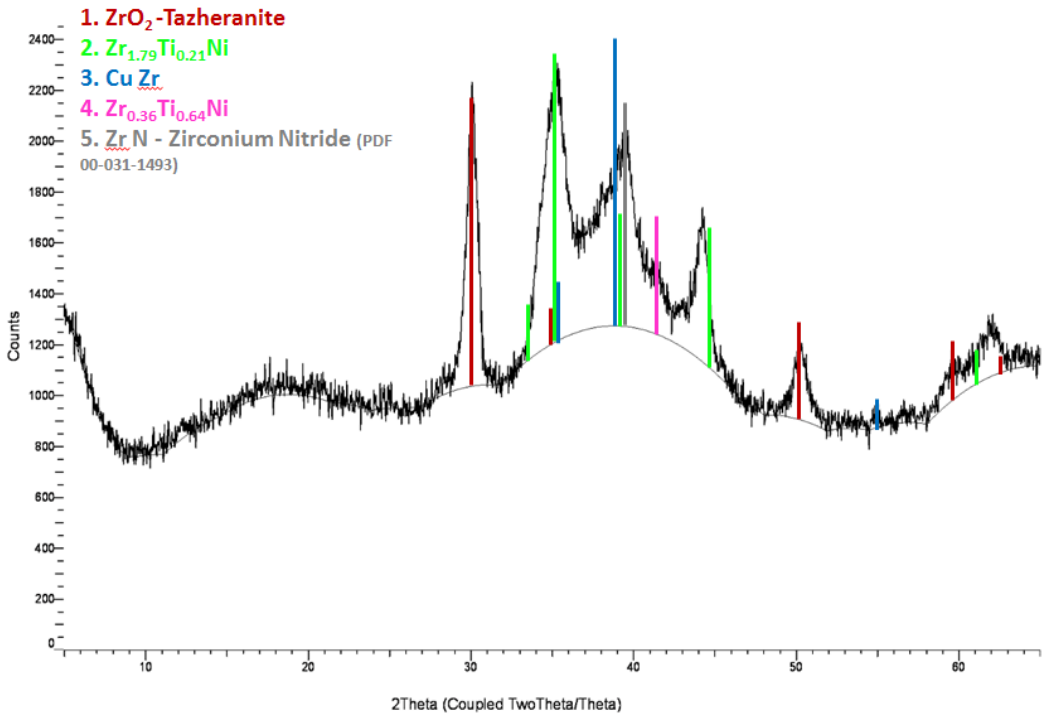

Figure 18. X-ray diffraction pattern of LM105 after heat treatment at 425°C for 30 minutes, showing the additional crystal formation of ZrN.

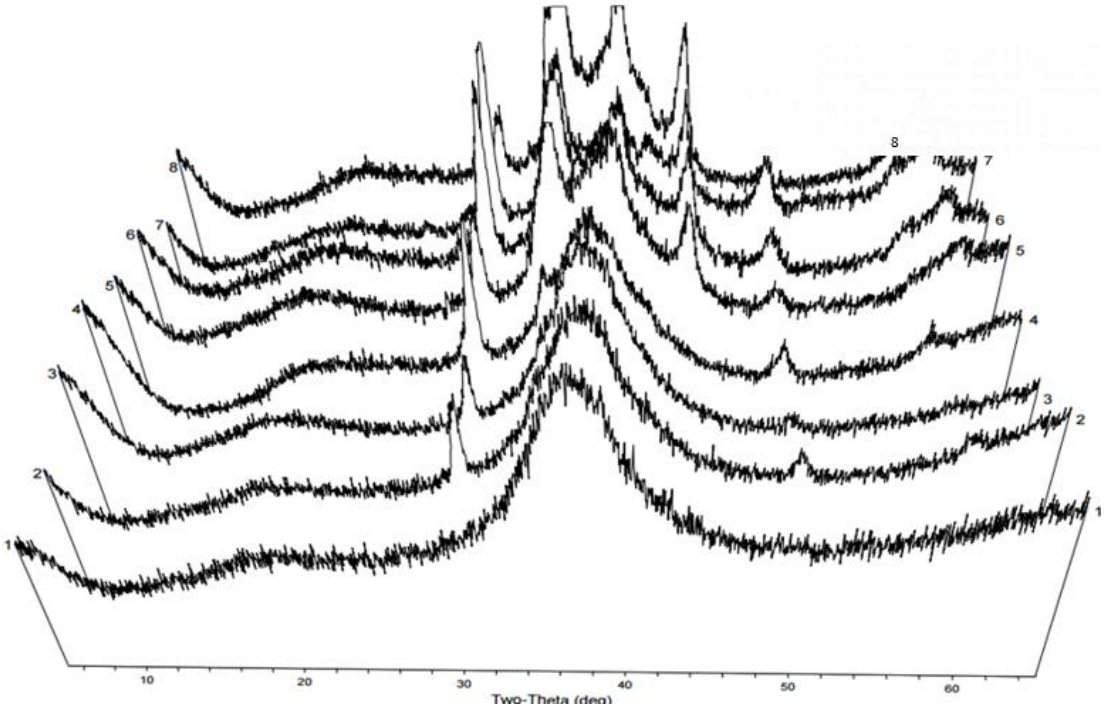

Figure 19. X-ray diffraction patterns aligned based on increasing time and temperature, as listed in Table VII.

Table VII: Samples used for Comparison of Crystallization Sequence in Figure 23.

Sample number, figure 17	Treatment Temp (°C)	Treatment Time (Min)	Average	StDEV	Figure Number
2	385	0	6.602	0.004	
3	385	15	6.596	0.011	
4	385	30	6.625	0.007	
5	405	30	6.696	0.006	
6	425	30	6.696	0.007	
7	445	30	6.696	0.006	
8	465	30	6.708	0.004	

"Somewhere between the amorphous glasses and the rigidly regimented periodic crystals lie the quasicrystal: ordered predictable, yet non-periodic arrangements of atoms."[14] It is possible that these crystallization that is occurring is in the form of crystallites or quasicrystals. Qualitative observations of Figure 19 shows that the unidentified peak at ~30° 2θ does not appear to broaden as it intensifies. This implies that the associated crystallites are not growing in size, merely in number[13]. This also appears

to be true for the CuZr peak, though it is somewhat convoluted by the secondary $Zr_{1.79}Ti_{0.21}Ni$ peak near 38° 2θ. All other peaks (those associated with Taxheranite, $Ti_{0.094}Ni_{0.906}$, and $Zr_{0.36}Ti_{0.64}Ni$) appear to broaden as they intensify. This may be a results of the slow conditions required for x-ray analysis. However, it is also possible that this broadening is due to an increase in crystallite size as the samples are heated for longer times and at hotter temperatures. Full crystallization of this glass should occur when these crystallites reach critical mass and act as nucleation sites for greater crystal growth.[13] This is only true if the crystallites (or other nucleation sites within the glassy matrix) exist while thermal and kinetic barrier are easily overcome. This occurs when the glass is held at high enough temperatures for long enough times for the full movement of surrounding ions.

B. Density Measurements

The density of sample set 1 was analyzed to understand the physical changes that occurred during heating. Samples treated at 385°C for 30 minutes showed the least overall variation, Figure 20. Because of this, 30 minutes was used as the baseline for analysis of the effect of temperature on density. Figure 21 shows the density of untreated samples, and those treated for 30 minutes from 385°C to 465°C. As expected, the density change is reduced above the glass transition temperature. This implies that the glass transition for LM105 lies somewhere between 385°C and 405°C. This confirms the DSC analysis showing transition at 398°C. Each set of data was also plotted independently, see Appendix D.

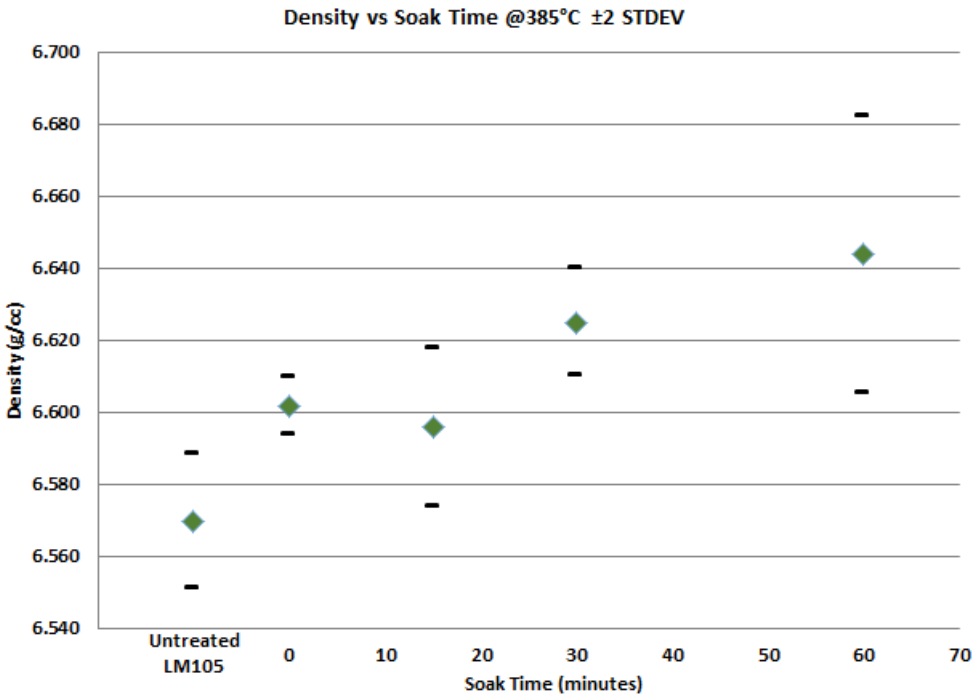

Figure 20. Density over time with ±2 standard deviation showing increased average density with increased soak time.

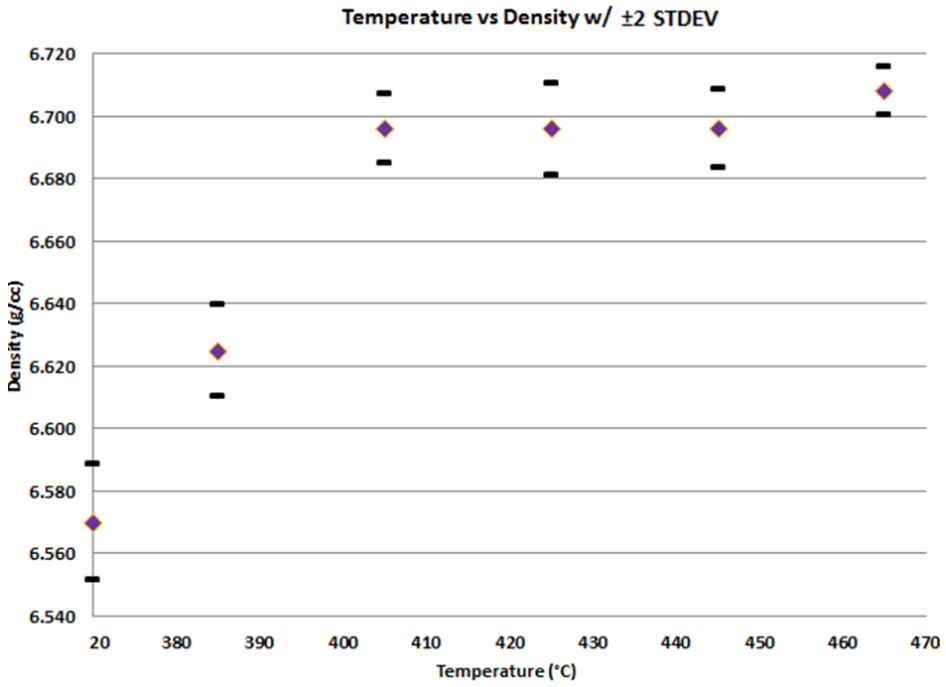

Figure 21. Density of samples treated for 30 minutes with ±2 standard deviation showing max density increase is obtained at 405°C.

When analyzing the density change vs. substrate used during treatment, there is a limited effect. Figure 22 shows the density for LM105 treated on each substrate for 30 minutes with two standard deviations. However, when analyzing the variability in the sample density vs. the substrate used, it becomes more apparent that samples treated on oxide substrates have the least variability, followed by graphite, then silicon nitrides, Figure 23. It is possible that this increase in variability with nitride samples is due to the high interaction of Ti or Zr with the nitrogen present in the substrate. Carbon would cause less variability than the nitride samples as the carbon acts as a getter for any O_2 in the atmosphere.

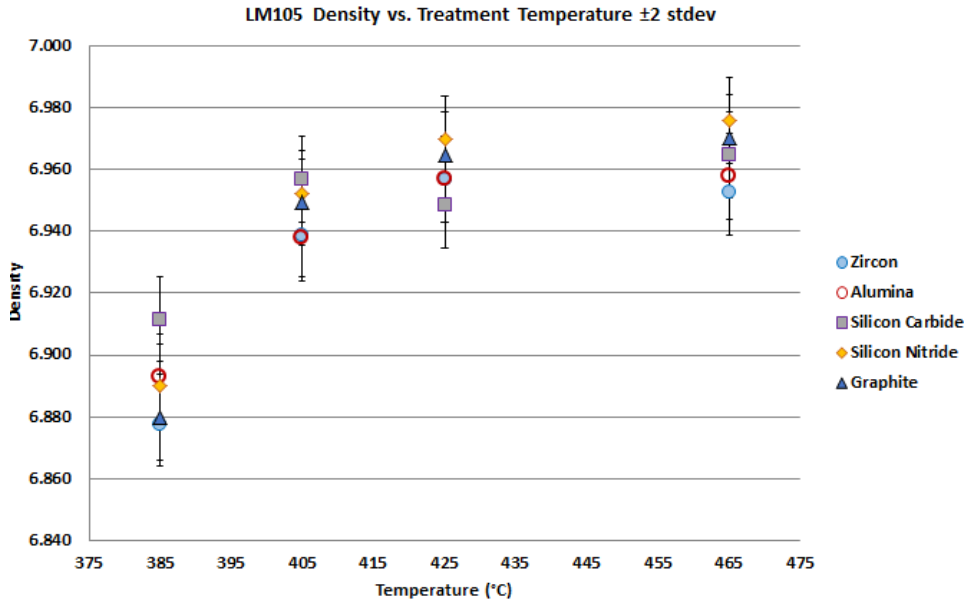

Figure 22. LM105 density ±2 standard deviations vs. substrate shows no change in glass density when placed on various substrates.

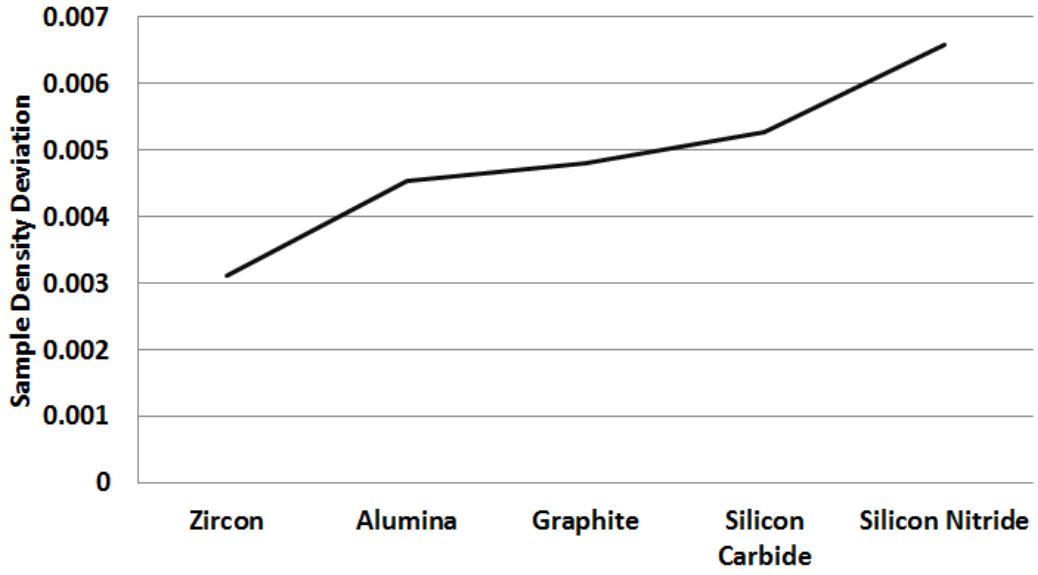

Figure 23. Average variability of density measurements by substrate shows increasing density variability when treated with carbon containing or nitrogen containing substrates.

C. SEM Imaging

1. LM105

SEM images taken of the LM105 alloy (non-amorphous) provided by LiquidMetal Technologies showed what appeared to be grain boundaries, Figure 24. For the fully amorphous samples, such as those exhibiting an x-ray diffraction pattern shown

in Figure 13, the surface showed no grain boundaries. The vertical marks observed here were created during counter gravity casting, Figure 25.

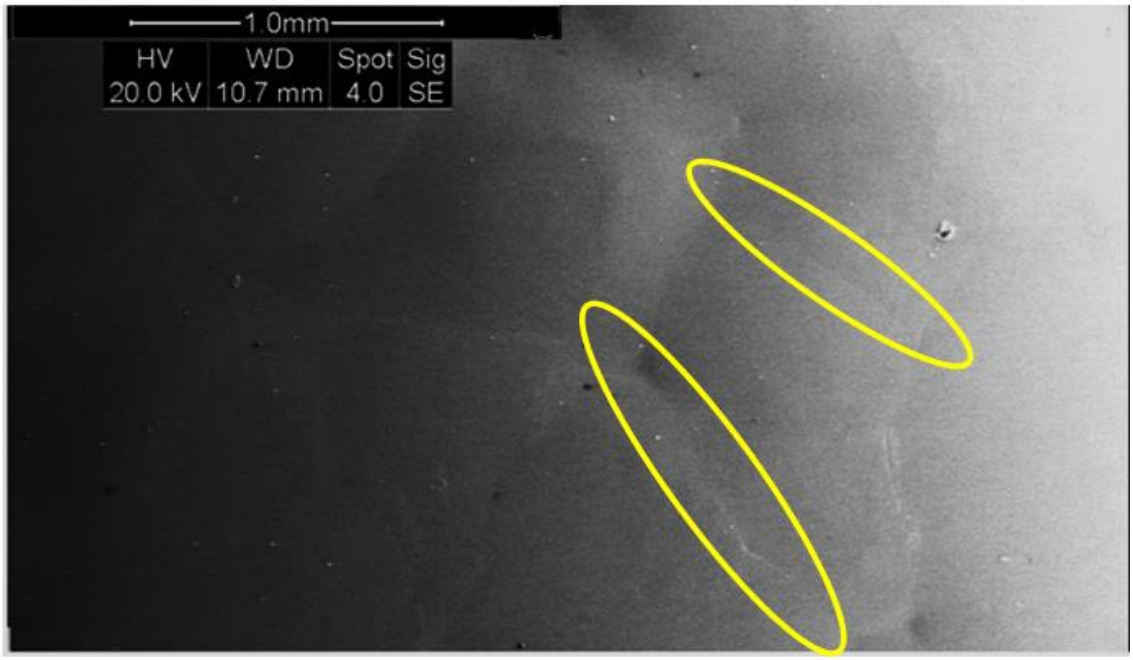

Figure 24. SEM Image of Crystalline LM105 Alloy. Highlighted regions showing grain boundaries.

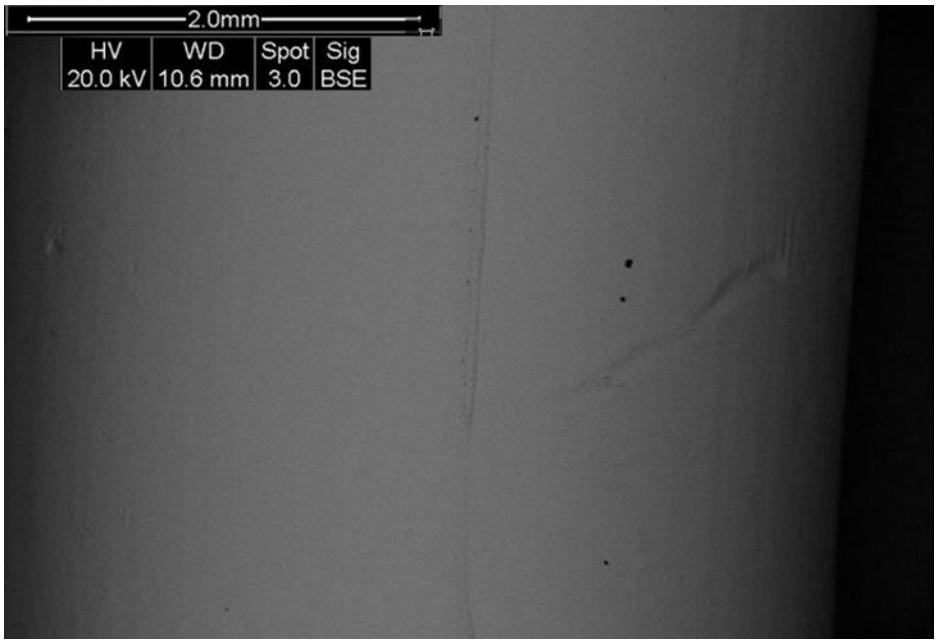

Figure 25. SEM image of fully amorphous LM105, with no apparent grain boundaries.

2. Zircon

Digital images of all samples are provided in Appendix E. It was important, however, to observe the same samples using SEM. Figure 26, for example, shows that there is an obvious interaction zone on the surface of zircon after being in contact with superheated LM105. Though it is obvious in the digital images, it was not known if the interaction reached below the surface. If this was caused by contaminants in the atmosphere that simply couldn't contact and interact with the surface where LM105 was blocking it, it could be seen in the SEM. Back scatter imaging, Figure 27, shows that this region of interaction does in fact reach lower than the top most layer of Zircon. The interacting region appear brighter suggesting that heavier elements are present in this area. It is likely caused by a loss of O_2 in this region, causing an increase in the relative zircon density. This may have occurred when oxygen interacted with the LM105. The hypothesized oxidation of the LM105 may be explained this way, but it was also present on the silicon carbide and silicon nitride samples. A cross sectional analysis, Figure 28, of this sample showed consistent Zircon grain structures and relative atomic densities outside of the interaction region, suggesting this was a local interaction.

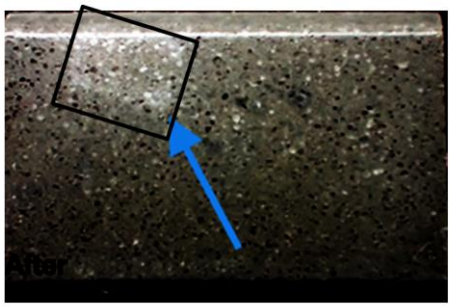

Figure 26. Digital image of Zircon substrate after heat treatment, square highlights the interaction region.

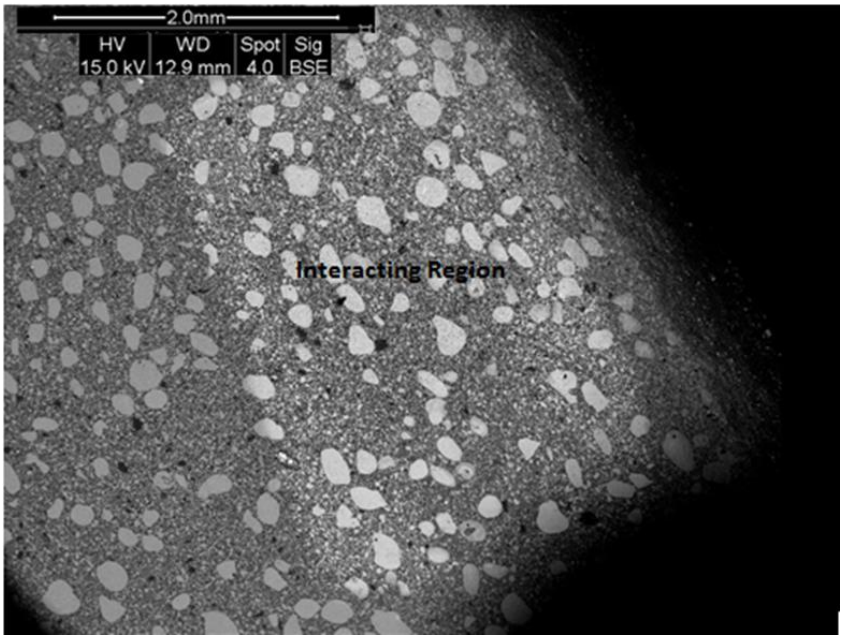

Figure 27. Top down view of overall zircon interaction region using BSE. The brighter region, where LM105 was placed on the surface, is representative of the heavier elements present.

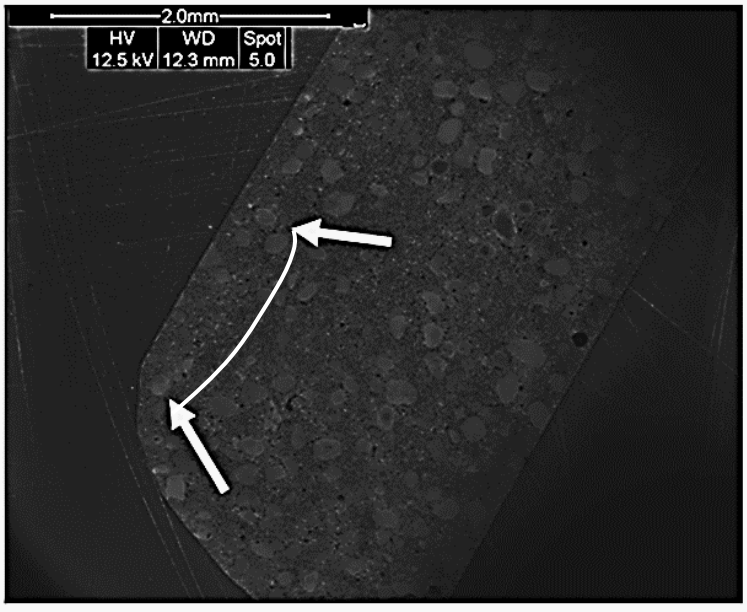

Figure 28. Zircon interaction zone cross section. The white arrows point to the corners of the interacting zone, and the line highlights the lower edge.

3. Alumina

The interaction of LM105 with alumina appears in the digital images as well, Figure 29. Upon further inspection with SEM imaging, it is apparent that there is a change in the

grain size at the interaction location, Figure 30. When examined via cross-sectional analysis, it can be seen that this change in grain size reached ~30μm into the material, Figure 31.

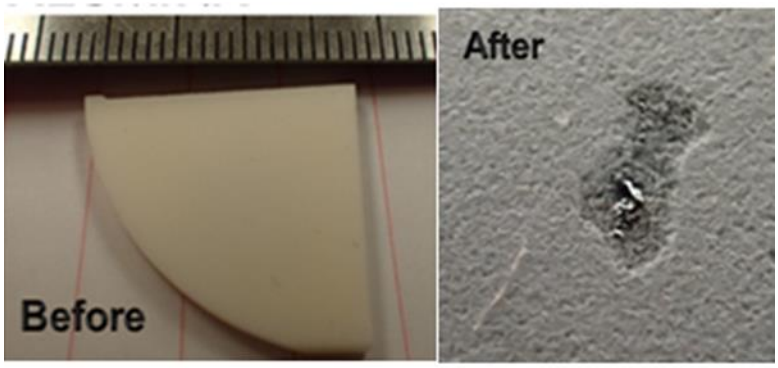

Figure 29. Alumina substrate before and after heat treatment.

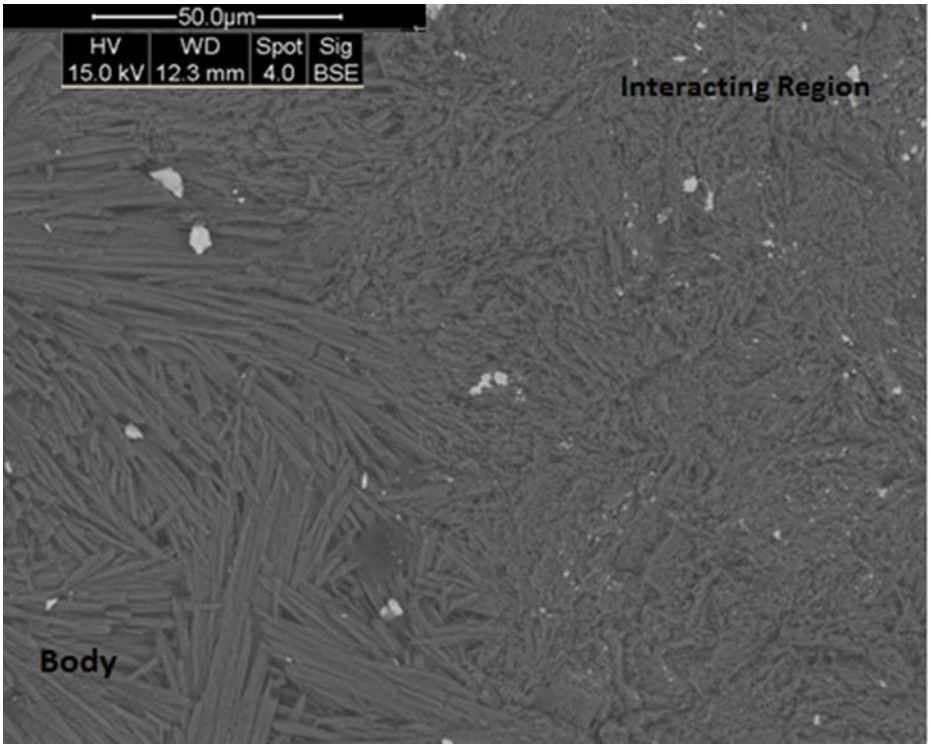

Figure 30. Top down view of alumina interacting region edge. Note the smaller grain size in the area of interaction.

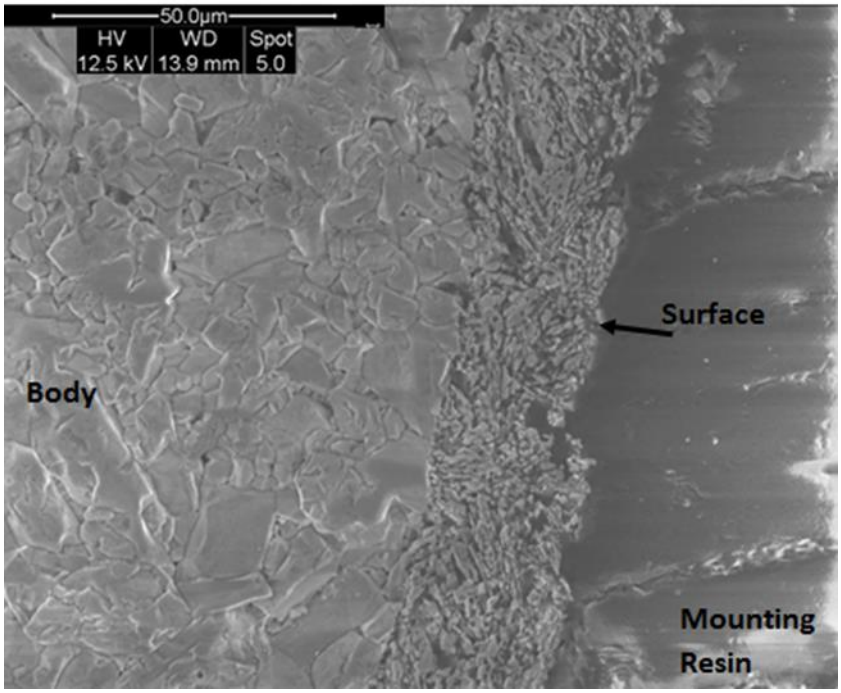

Figure 31. Alumina cross section showing clear grain size change in interacting region.

4. Measured Corrosion Distance

The maximum depth of interaction for each sample was measured as demonstrated in Figure 32. The Zircon sample showed no depth of attack in cross section, simply a change in the atomic density in the area of interaction, Figure 27. Each sample was measured 20 times. The average maximum depth and standard deviation are listed in

Table VIII. The 20 measurements taken were done so in a random order in an attempt to remove operator measurement bias. The resultant measurements showed some variation, but all were less than 8.5µm in standard deviation.

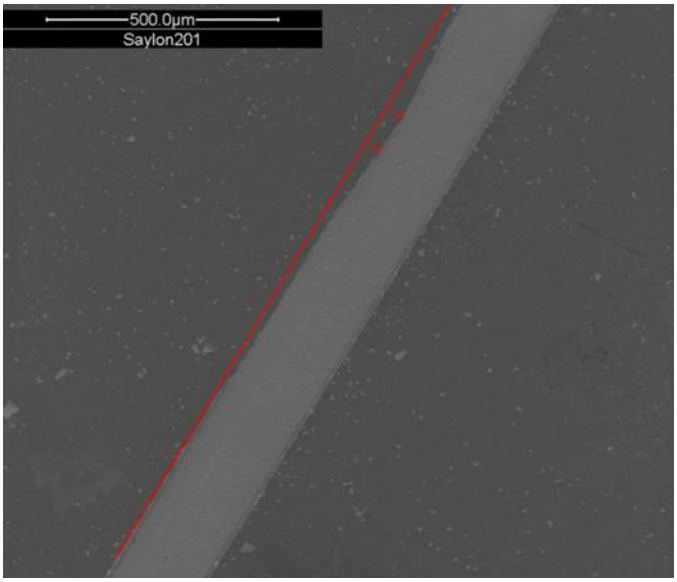

Figure 32. Example of depth of interaction between Syalon 201 substrate and superheated LM105. The red line shows initial surface location.

Figure 33 shows a box plot comparison of corrosion depth for all samples measured. It is clear from this plot that Syalon 110 (S110) had the highest interaction depth. This sample was removed and depths were plotted again in Figure 34. It is clearer, with this comparison, that Syalon 201 (S201 interaction depth), had statistically less interaction than all other samples.

Table VIII: Substrate Maximum Corrosion Depth (20 readings each)

Substrate	Average Interaction Depth (µm)	Standard Deviation (µm)
Alumina	37.22	1.63
Silicon Nitride	32.48	0.50
Syalon 050	33.40	0.50
Syalon 101	33.86	1.53
Syalon 110	76.32	8.40
Syalon 201	27.20	1.15

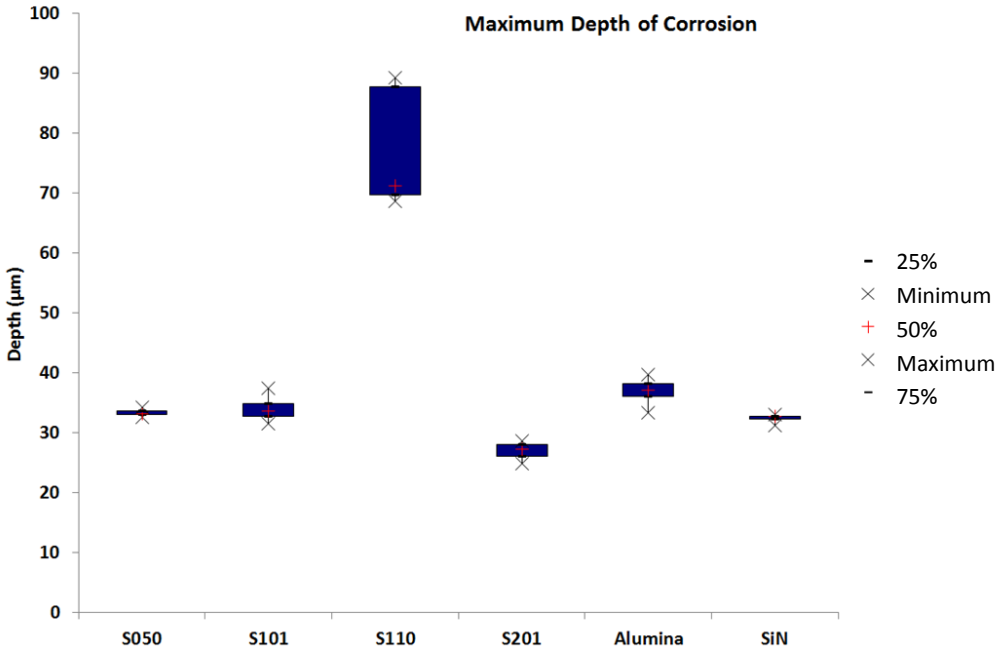

Figure 33. Box plot comparison of corrosion depth, note the high Syalon 110 corrosion depth and variability.

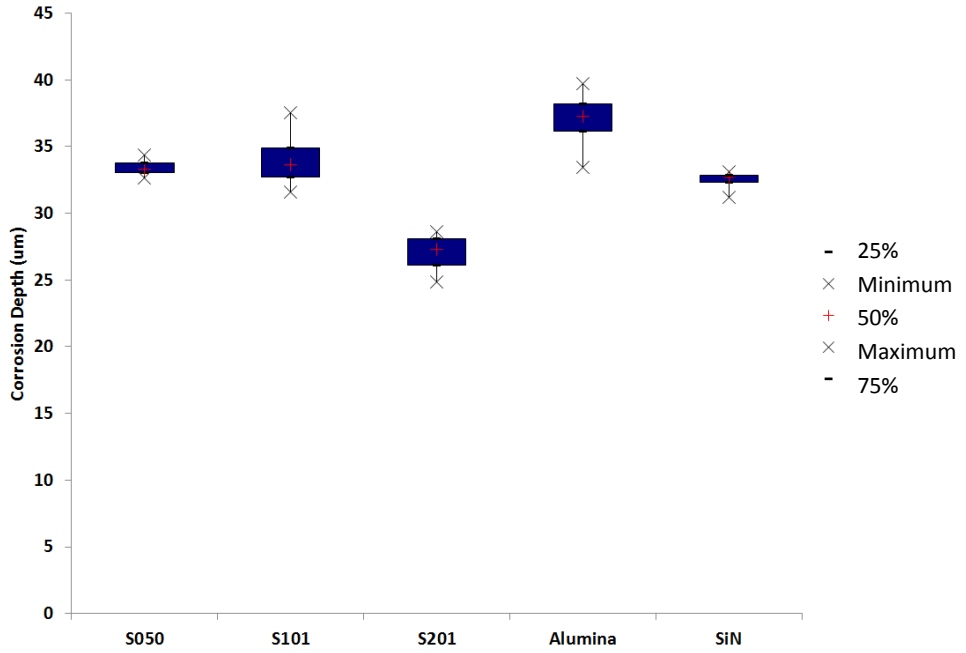

Figure 34. Box plot comparison of corrosion depth showing Syalon 201 as least corroded.

CONCLUSIONS AND FUTURE WORK

A. Crystallization behavior of LM105 and possible conclusions

The crystallite formation in LM105 suggests that is possible to create a composite material with a variety of Zr/Ti crystallites in a metallic glass matrix via the heat treatment of fully amorphous LM105. The inclusion of these crystallites should lead to a change in physical properties including hardness, strength, electrical conductivity, corrosion, and even ductility. By studying these physical changes, it may be possible to optimize heat treatment of LM105 to create desired properties for a variety of applications. Further study of the glass transition zone of LM105 may also lead to greater insight into the bonding behavior of metallic glasses. The formation of these crystallites may suggest that there are covalently bound species within the largely metallic and glassy matrix.

B. Best material for crucible melting

Through the simple technique of creating an extreme environment for the interaction of superheated LM105 and a variety of substrates, it was possible to see that the zircon material tested underwent the least corrosion. This is most likely due to the high level of Zr present in both the metallic glass and the substrate. The inability for the zircon to interact with the already bound oxygen may also be a contributing factor in its resistance to corrosion by this specific glass. However, it is also apparent that it had a fairly deep level of interaction. It is unclear as to how this will affect the behavior of the zircon as far as re-use and physical property changes. Further testing on the affected zircon material is required before use in industrial applications. Bulk testing of zircon (in situ with the production process) would give the best insight into industrial use. It is suggested that both Zircon and Syalon201 would undergo further testing. Though the sessile drop test could offer a more conclusive result for the interaction of molten LM105, the action of superheating LM105 also gives good insight into the real-world interactions seen during product formation of LM105.

C. Future Work

A comparison of properties for samples undergoing a fast or slower heat cycle could lead to interesting learnings. With faster ramping speeds it may be create more, smaller crystallites. This would likely change the physical and chemical properties of the metallic glass. It would also be beneficial to investigate the position of ions within grains of fully crystallized alloys. This should be done via the re-heating method for comparison to the as cast non-glassy alloy. This should give insight into the bonding nature of the metallic glass. The grain boundaries and core of grains should be measured. This will give insight into the ionic movement during cooling. The existence of higher concentration of alumina near grain boundaries would imply that it is one of the last elements to leave the glass matrix for a crystalline structure. Should this process be stopped mid-crystallization, and the glassy matrix left behind is alumina rich, perhaps the crystalline regions etched away to leave behind a metallic glass that could otherwise not be formed.

REFERENCES

[1] Suryanarayana, C., and A. Inoue, *Bulk Metallic Glasses* 1st ed., Vol. 1; Ch. 2-4 41-147. CRC Press Taylor & Francis Group, Bsuroca Raton, FL, 2011.

[2] Duwez, P. "Metallic Glasses – Historical Background," *Top. Appl. Phys.* **46** 19-23 (2005).

[3] Jaiswal, Abhishek, Andrey Podlesynak, Georg Ehlers, Rebecca Mills, Stephanie O'Keeffe, Joseph Stevick, James Kemption, et al. "Coincidence of Collective Relaxation Anomaly and Specific Heat Peak in Bulk Metallic Glass-Forming Liquid," *Phys. Rev. B*, **92** [2] 024202 (2015).

[4] Chang, Y. Hongbo Cao, Dong Ma, Ling Ding, Ker-Chang Hsieh "Zirconium-Rich Bulk Metallic Glass Alloys," U.S. Pat. 7,368,023 B2. May 2008.

[5] Antaonysamy, Alphons Anadaraj, Simon Pauly, Briji Kumar Dhindaw, and Jurgen Eckert, "Influence of Superheat on Microstructure and Mechanical Properties of Ductile Cu47.5Zr47.5Al5 Bulk Metallic Glass-Matrix Composite," *J. Mater. Eng. Perform.*, **20** [7] 1196-1205 (2010).

[6] Waniuk, Theodore A., Josepth Stevick, Sean O'Keefe, Stratton J. Dermot, Josepth C. Poole, Matthew S. Scott, and Christopher D. Prest. "Counter Gravity Casting of Hollow Shapes," U.S. Patent 8,701,742 B2. September 2012.

[7] Dong, Wenbo, Haifeng Zhang, Wensheng Sun, Bingzhe Ding, and Zhuangqi Hu, "Formation, Thermal Stability and Mechanical Properties of Zr-Nb-Cu-Ni-Al Bulk Metallic Glasses," *Mater. Trans.*, **47** [5] 1294 – 1298 (2006).

[8] Kuhn, U., J. Eckert, N. Mattern, and L. Shultz, "ZrNbCuNiAl Bulk Metallic Glass Matrix Composites Containing Dendritic BCC Phase Precipitates," *Appl. Phys. Lett.*, **80** [14] 2478-2480 (2002).

[9] "EASYHEAT Induction Heating Systems" (2016) Ambrell Accessed on: August 2016. Available at <https://www.ambrell.com/easyheat-systems>

[10] Stull D. R. and H. Prophet,"JANAF Thermochemical Tables, NSRDS-NBS 37" US Dept. Of Commerce, National Bureau of Standards, 1971. As cited in Stanley M. Howard "Ellingham Diagrams" SD School of Mines and Technology. Access on January 2017. Available at <http://showard.sdsmt.edu/MET320/Handouts/EllinghamDiagrams/Ellingham_v22_Macro.pdf>

[11] Finck, Didier, and Dieter Heumannskaemper, "Matching Your Crucible to Your Application," (2016) *Morgan Advanced Materials, Morgan Molten Metal Systems* Accessed on October 2016. Available at <http://www.morganmms.com/en-gb/resources/technical-articles/matching-your-crucible-to-your-application/>

[12] Yuan, Yuehua and T. Randall Lee, "Contact Angle and Wetting Properties"; 1-30 in Surface Science Technologies Vol. 1 Springer Berline (2013).

[13] Speakman, Scott A. n.d. "X-ray Diffraction Shared Experimental Facility," (2016) *MIT center for Materials Science and Engineering* Accessed on: October 2016 Available at <http://www.google.com/url?sa=t&rct=j&q=&esrc=s&source=web&cd=1&ved=0ahUKEwi-6Pm4sNXPAhUDJB4KHSowDiUQFggeMAA&url=http%3A%2F%2Fwww.ncl.ac.uk%2Facma%2Fresources%2Fdocuments%2FMIT_CrystalSizeAnalysis_SpeakmanS.pptx&usg=AFQjCNHYCrj7RLwm2KOp5rYpb3MAmnubHg&si>

[14] Steinhardt P.J. "Solid-state Physics – How does your Quasicrystal Grow?" *Nature* **452** [7183] 43-44 (2008).

[15] "What are Sialon Ceramics?" (2001) *International Syalons (Newcastle) Limited* Accessed on: July 2016. Available at <http://www.syalons.com/resources/advanced-ceramic-articles-and-guides/guide-to-types-of-sialon-ceramics/>

[16] "Guide to Types of Sialons" (2016) *Advanced Ceramic Solutions for Extreme Environments* Accessed on Oct 2016 Available at <http://www.syalons.com/resources/advanced-ceramic-articles-and-guides/guide-to-types-of-sialon-ceramics/>

APPENDIX

A. Carbolite Furnace Diagrams

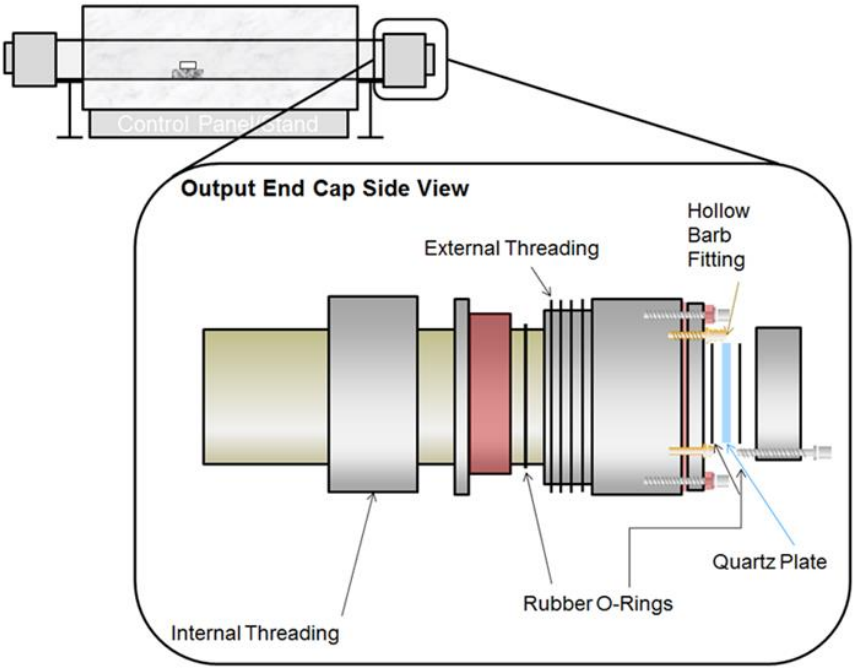

Figure 35. Carbolite Furnace End Cap Construction Diagram.

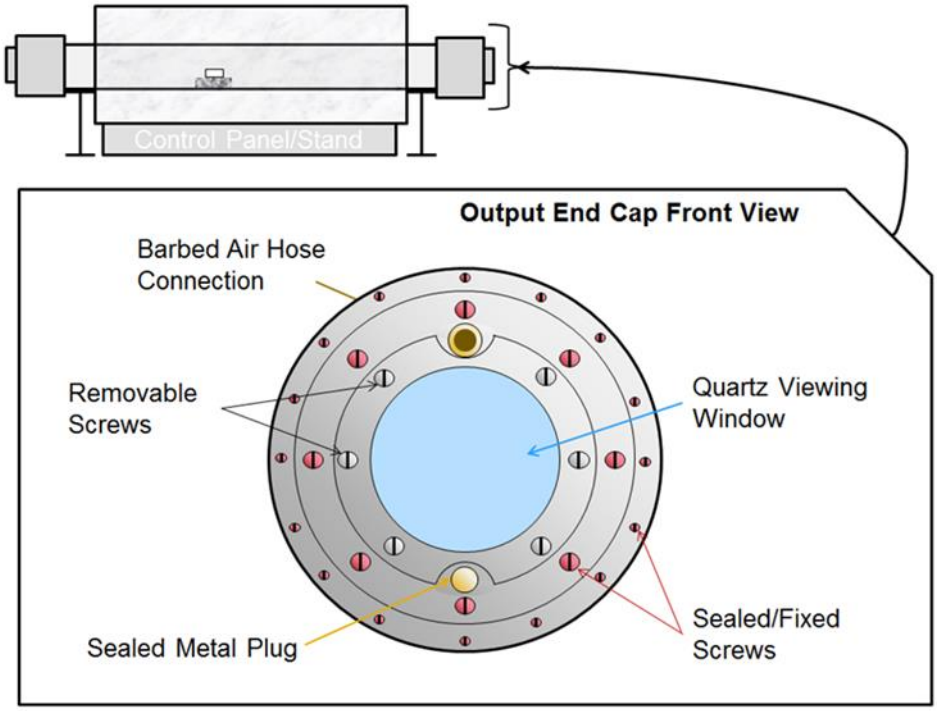

Figure 36. Carbolite Furnace Viewing Port and gas exhaust.

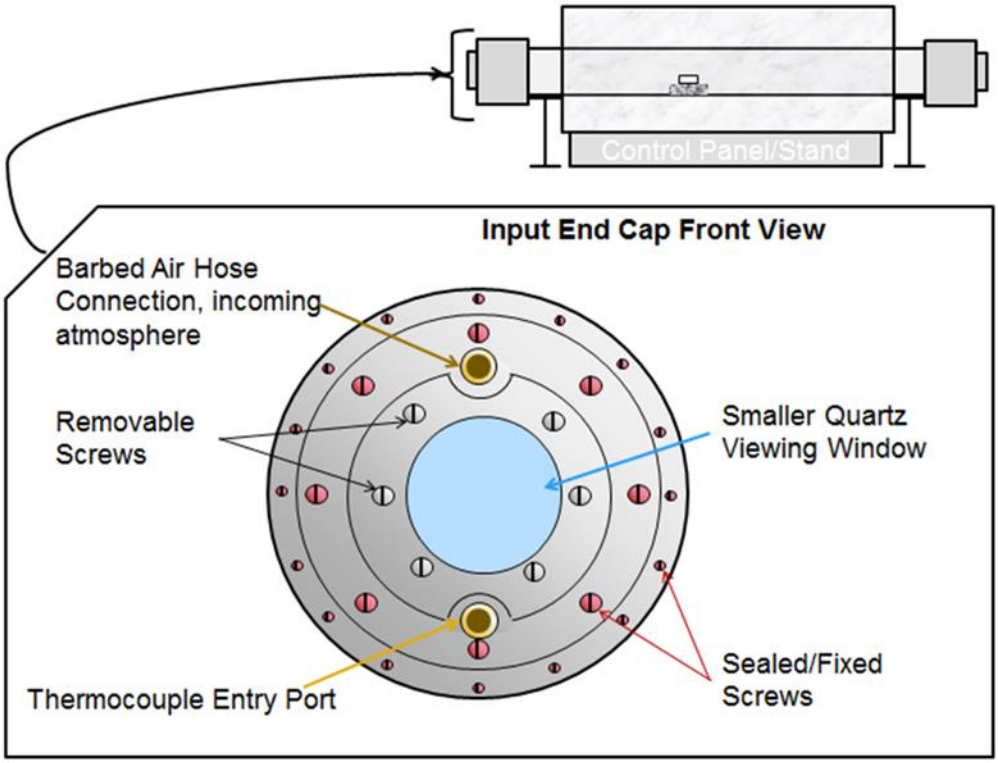

Figure 37. Carbolite Furnace Gas Inlet and Thermocouple location.

B. Substrate Material information [15,16]

Physical property data for Syalon 101

Property	Value	Units
Composition	β-Sialon	-
Density	3.24	g/cc
Porosity	0	%
3 point Modulus of Rupture at 20°C (Specimen 3 × 3 × 50mm, span 19.05mm)	945	MPa
3 point Modulus of Rupture at 1000°C	700	MPa
Weibull Modulus	15	-
Compressive Strength	>3500	MPa
Young's Modulus of Elasticity	288	GPa
Poisson's Ratio	0.23	-
Hardness (HRA)	92	-
Hardness (Vickers Hv_{50})	14.71 (1500)	GPa (Kg/mm^2)
Fracture Toughness K_{1C}	7.7	MPa $m^{½}$
Thermal Expansion Coefficient (0-1200°C)	$3.0X10^{-6}$	K^{-1}
Thermal Conductivity	28	W/(mK)
Specific Heat	650	J/kg/K
Thermal Shock Resistance	900	ΔT°C quenched in cold water
Maximum Use Temperature	1200	°C
Electrical Resistivity	10^{12}	ohm cm
Dielectric Constant	8.1	-
Loss Tangent (10GHz)	0.0019	-

Physical property data for Syalon 110

Property	Value	Units
Composition	β-Sialon/BN	-
Density	2.65	g/cc
Porosity	10	%
3 point Modulus of Rupture at 20°C (Specimen 3 × 3 × 50mm, span 19.05mm)	500	MPa
3 point Modulus of Rupture at 1000°C	400	MPa
Weibull Modulus	10	-
Young's Modulus of Elasticity	139	GPa
Poisson's Ratio	0.19	-
Hardness (HRA)	88	-
Hardness (Vickers Hv_{50})	11.77 (1200)	GPa (Kg/mm^2)
Fracture Toughness K_{1C}	3.5	MPa $m^{½}$
Thermal Expansion Coefficient (0-1200°C)	$3.0X10^{-6}$	K^{-1}
Thermal Conductivity	27.0	W/(mK)
Thermal Shock Resistance	800	ΔT°C quenched in cold water
Maximum Use Temperature	1450	°C
Electrical Resistivity	10^{12}	ohm cm

Physical property data for Syalon 201

Property	Value	Units
Composition	β-Sialon	-
Density	3.24	g/cc
Porosity	0	%
3 point Modulus of Rupture at 20°C (Specimen 3 × 3 × 50mm, span 19.05mm)	825	MPa
3 point Modulus of Rupture at 1000°C	750	MPa
3 point Modulus of Rupture at 1350°C	600	MPa
Weibull Modulus	10	-
Young's Modulus of Elasticity	290	GPa
Poisson's Ratio	0.23	-
Hardness (HRA)	92.7	-
Hardness (Vickers Hv_{50})	16.18 (1650)	GPa (Kg/mm^2)
Fracture Toughness K_{1C}	4.5	MPa $m^{½}$
Thermal Expansion Coefficient (0-1200°C)	$3.0X10^{-6}$	K^{-1}
Thermal Conductivity	21	W/(mK)
Thermal Shock Resistance	600	ΔT°C quenched in cold water
Maximum Use Temperature	1450	°C
Electrical Resistivity	10^{12}	ohm cm

C. Digital Photographs of Sample Set 2

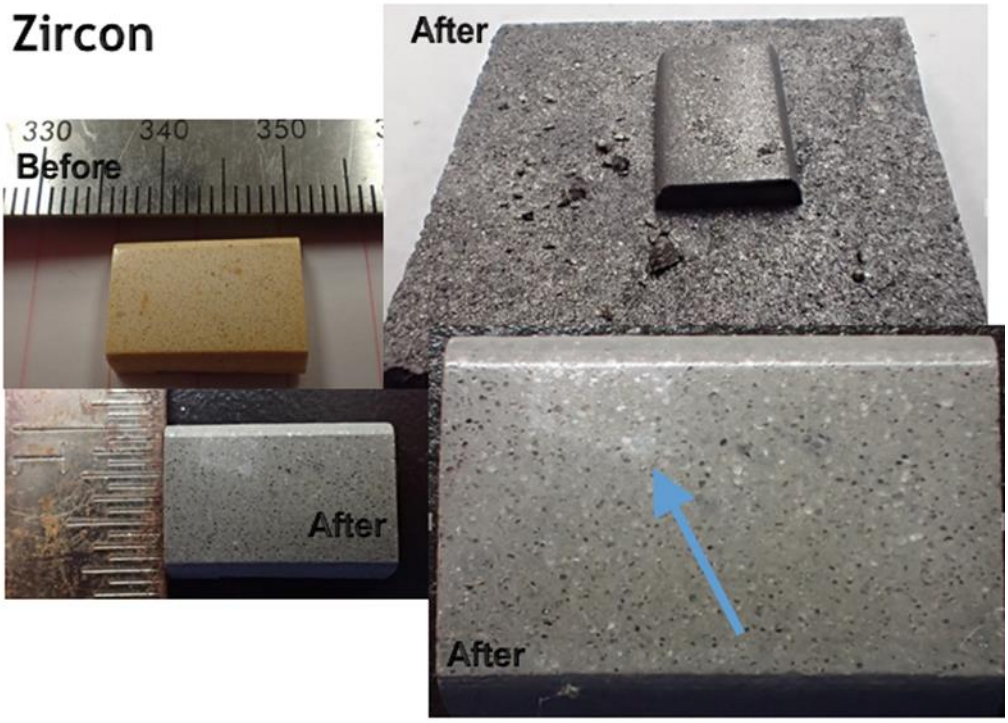

Figure 38. Zircon digital images before and after heat treatment.

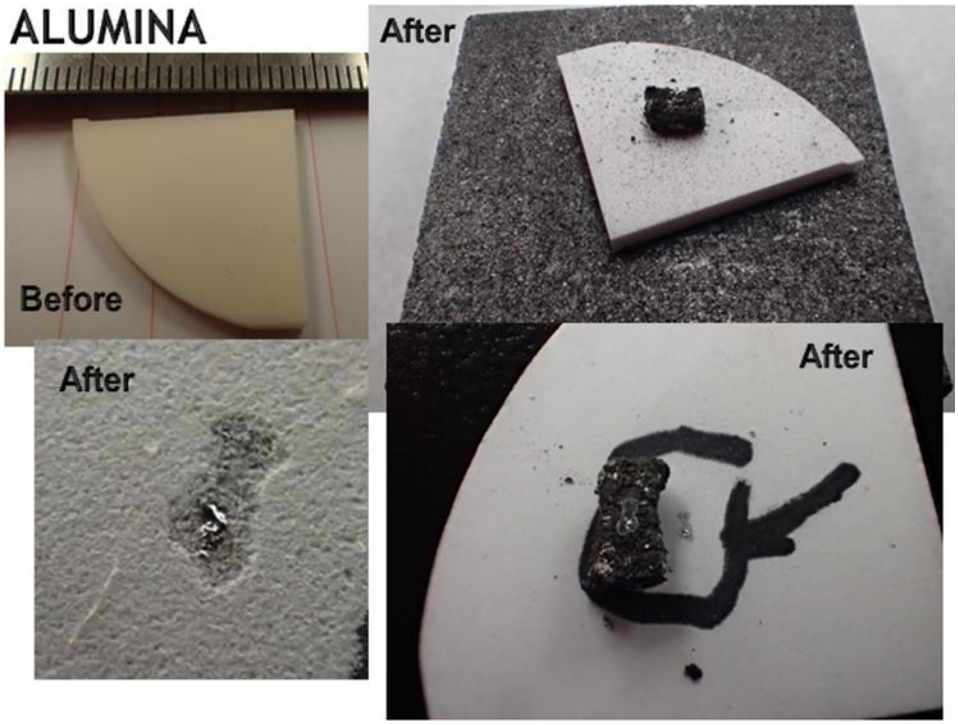

Figure 39. Alumina digital images before and after heat treatment.

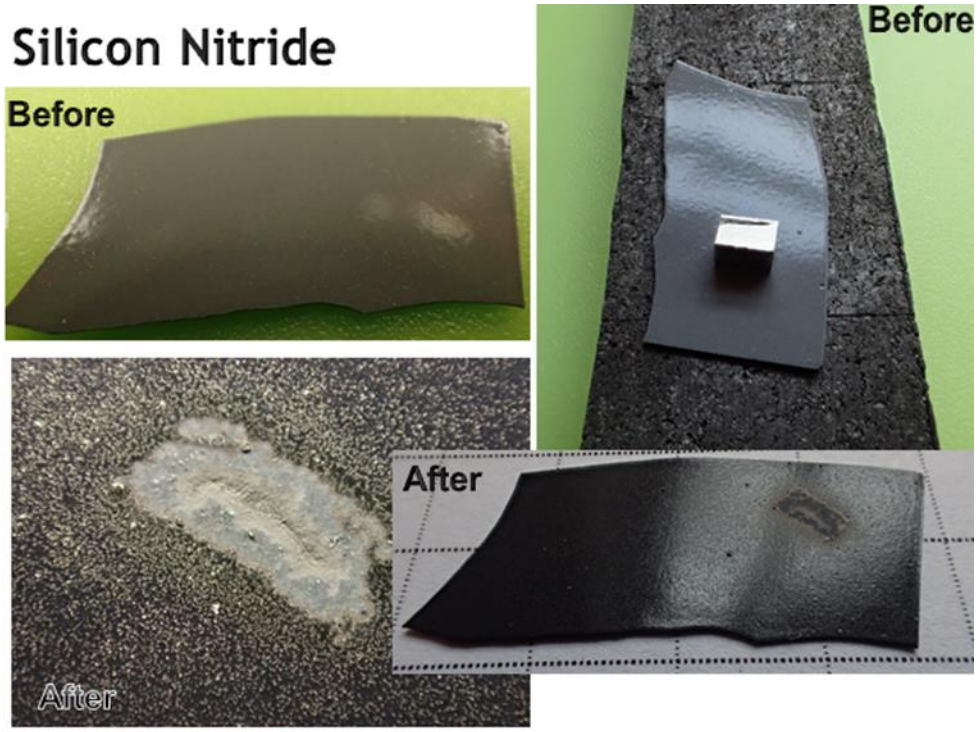

Figure 40. Silicon Nitride digital images before and after heat treatment.

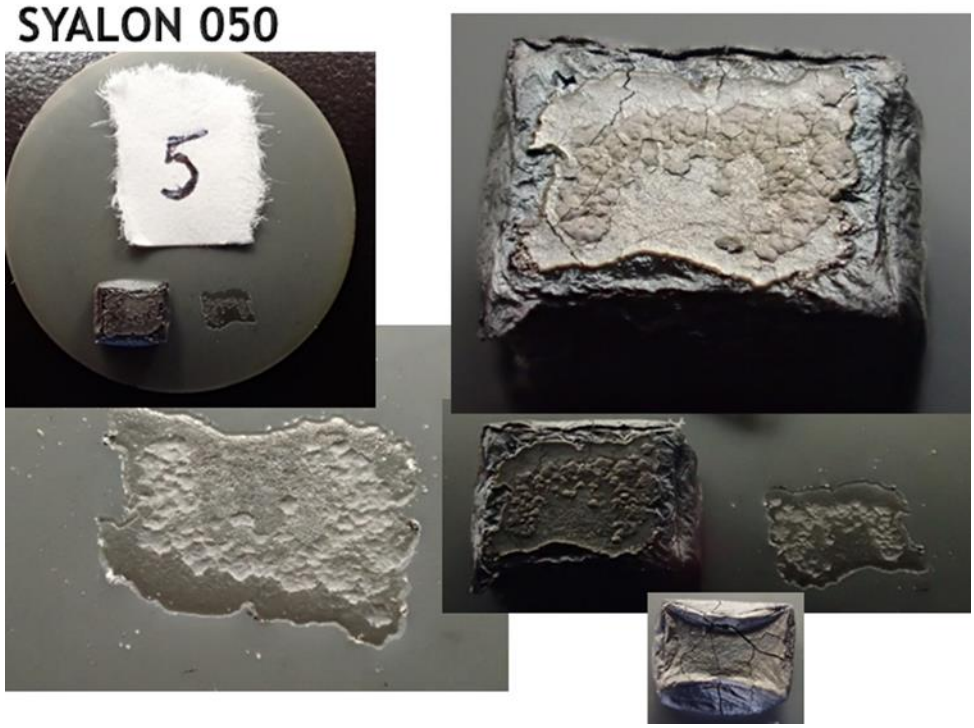

Figure 41. SYALON 050 digital images after heat treatment.

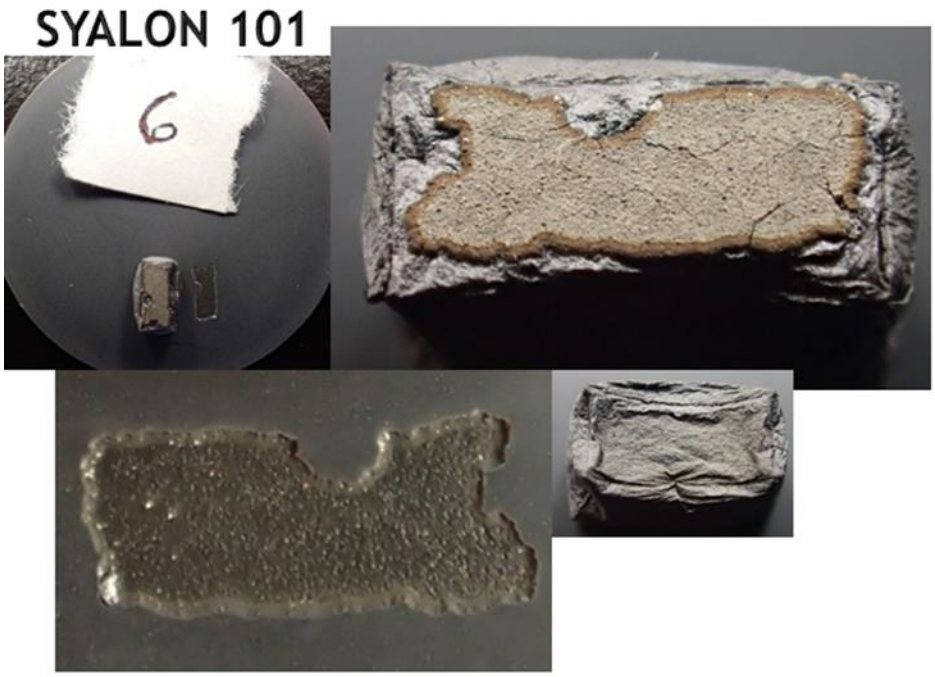

Figure 42. SYALON 101 digital images after heat treatment.

Figure 43. SYALON 110 digital images after heat treatment.

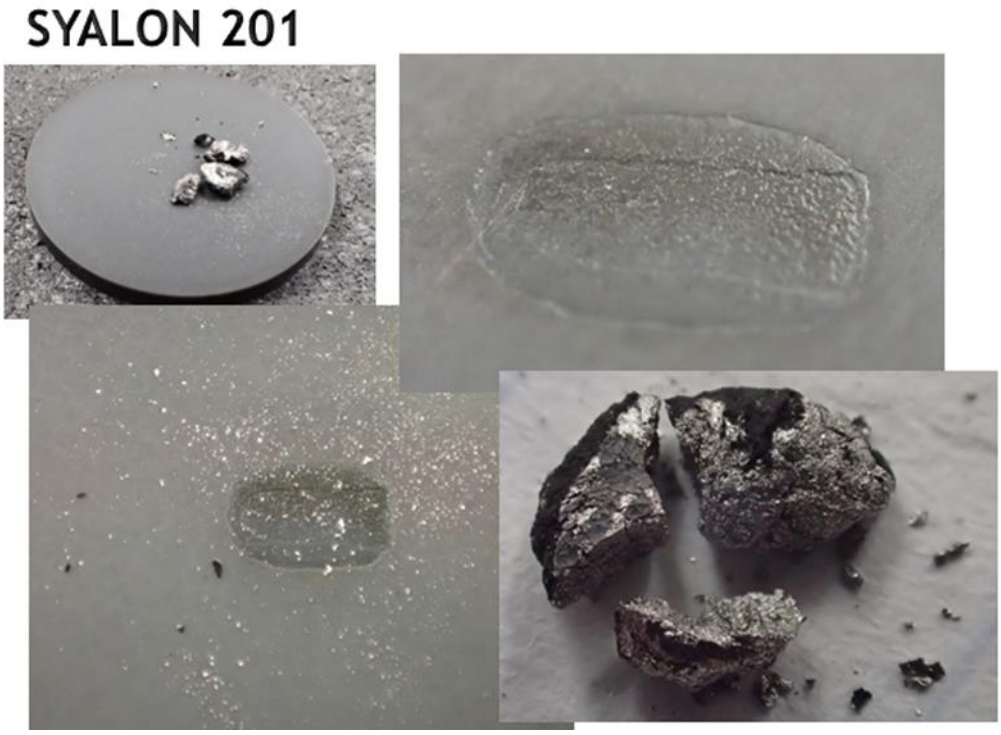

Figure 44. SYALON 201 digital images after heat treatment.

D. Density Measurement Data Plots

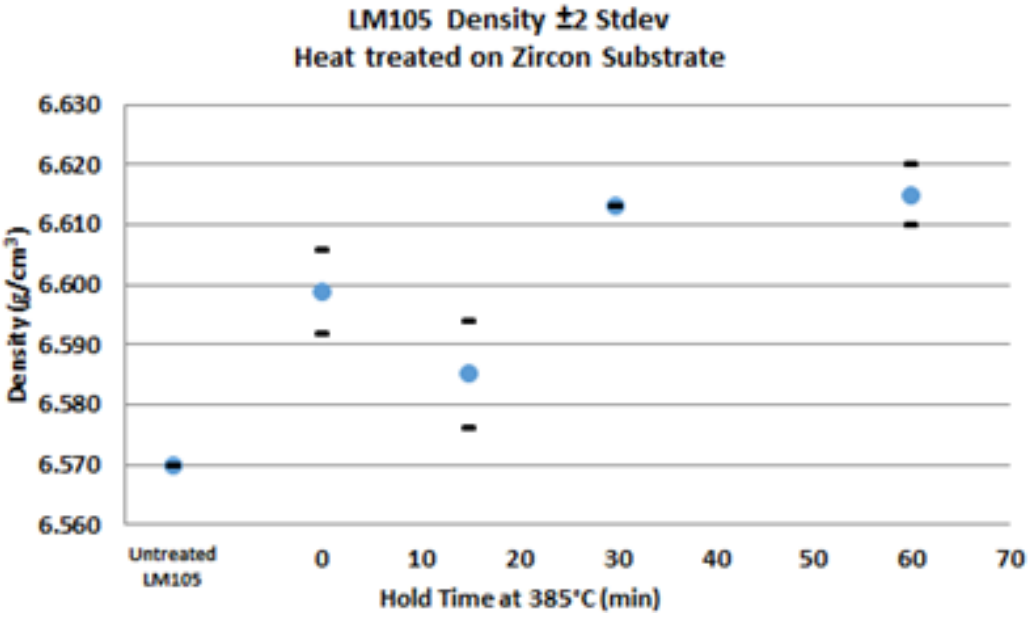

Figure 45 LM105 Density +-2 standard deviations when treated on zircon substrate at 385°C.

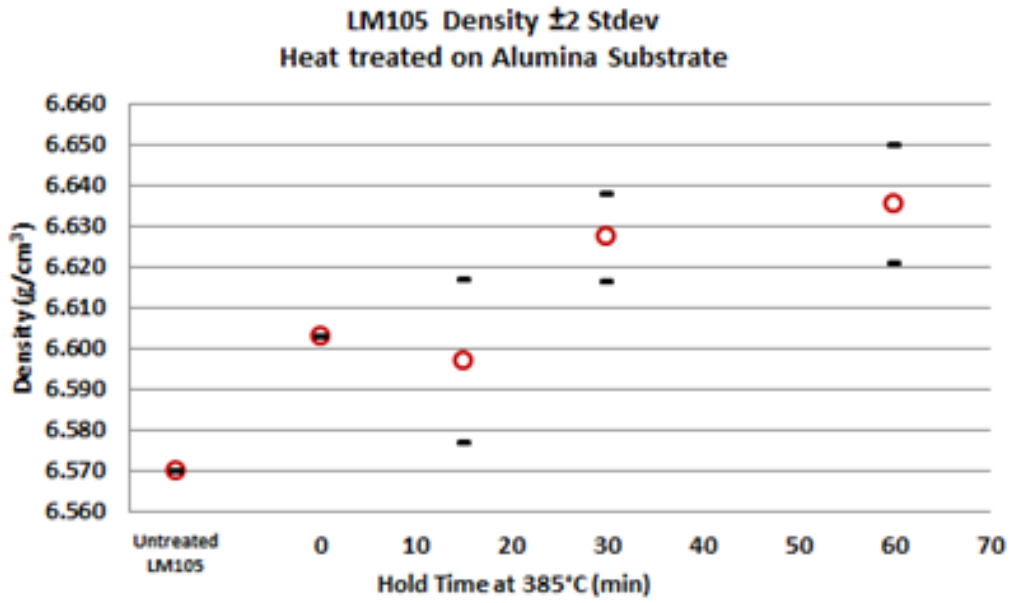

Figure 46. LM105 Density +-2 standard deviations when treated on alumina substrate at 385°C.

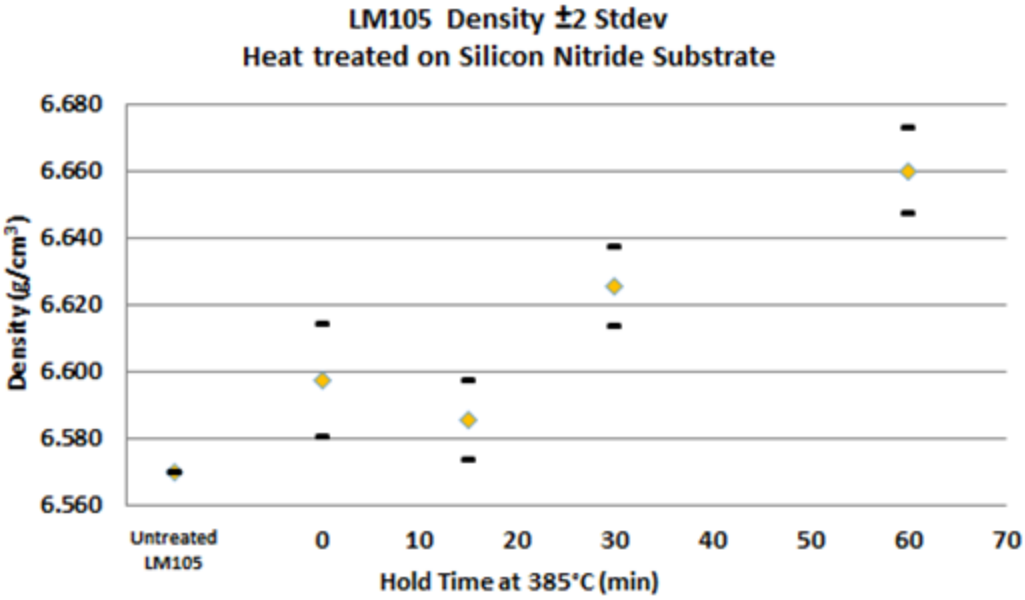

Figure 47. LM105 Density +-2 standard deviations when treated on silicon nitride substrate at 385°C.

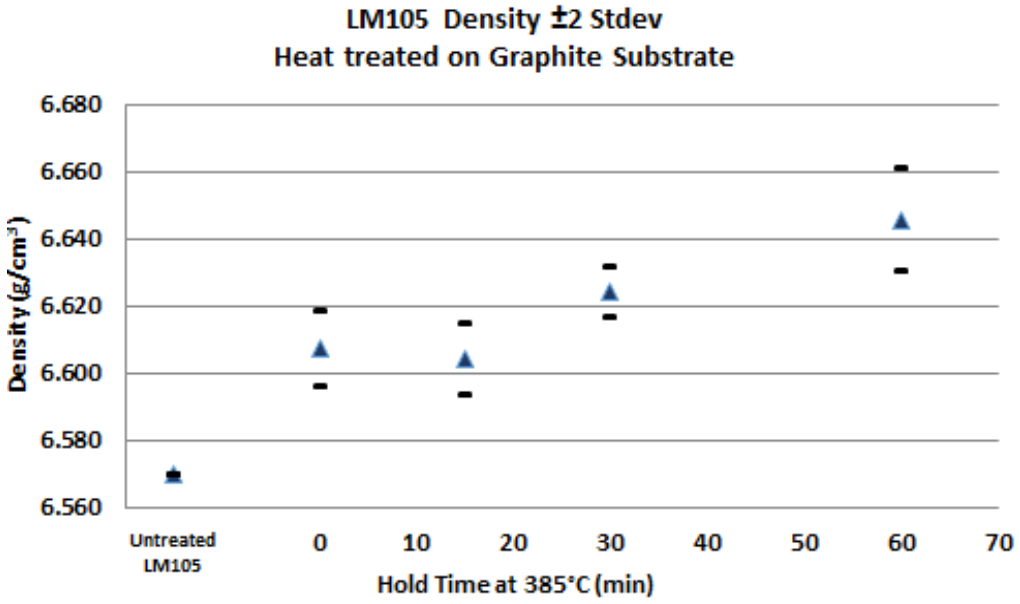

Figure 48. LM105 Density +-2 standard deviations when treated on graphite substrate at 385°C.

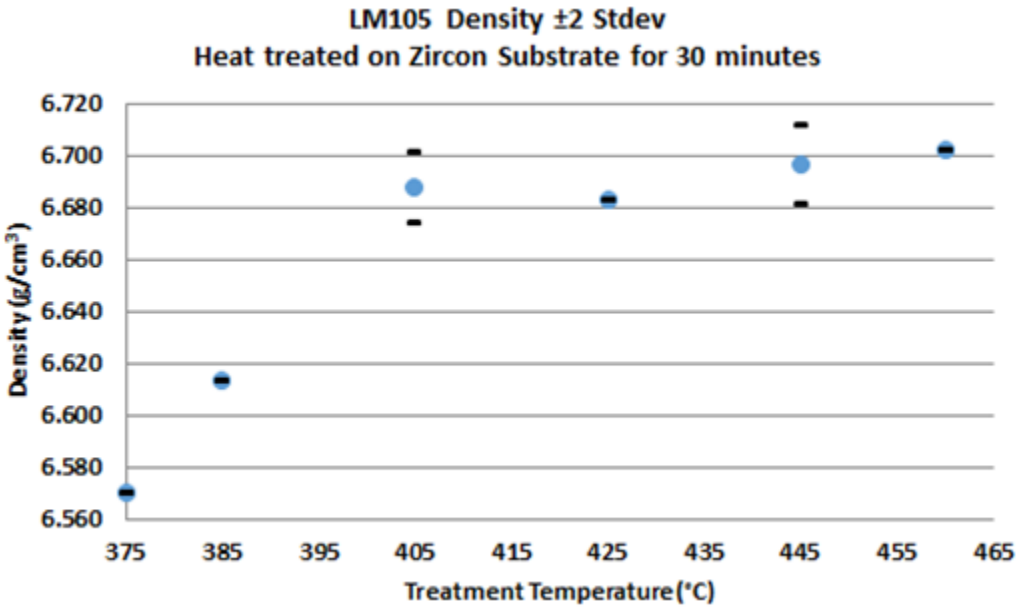

Figure 49. LM105 Density +-2 standard deviations when treated on zircon substrate for 30 minutes.

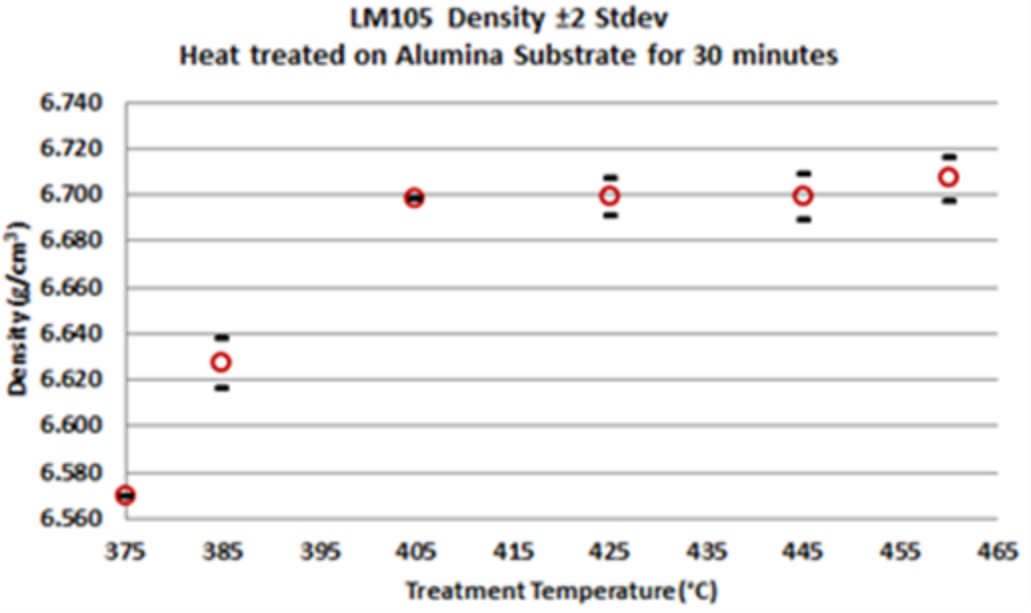

Figure 50. LM105 Density +-2 standard deviations when treated on alumina substrate for 30 minutes.

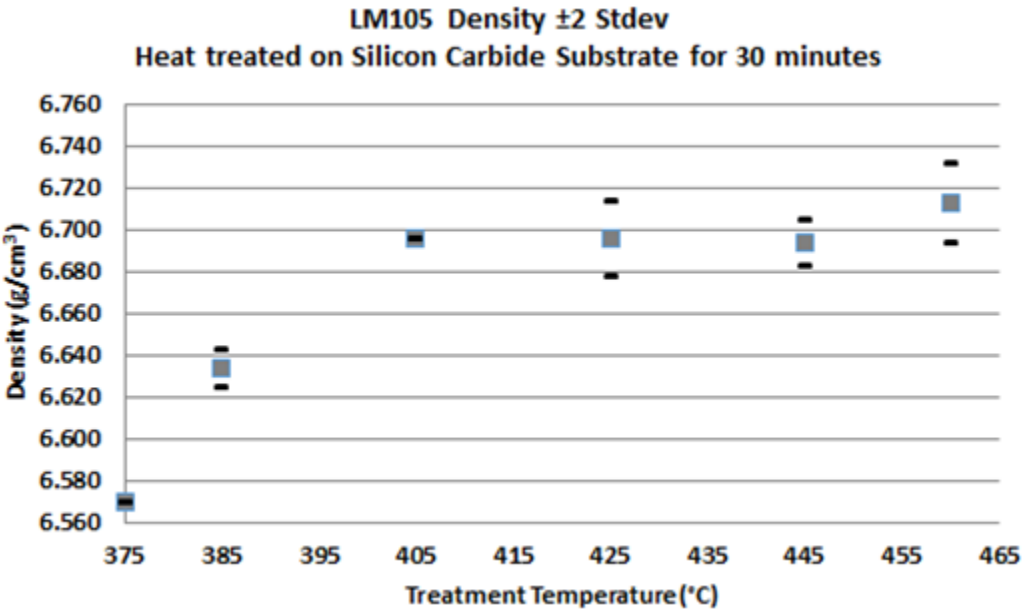

Figure 51. LM105 Density +-2 standard deviations when treated on silicon carbide substrate for 30 minutes.

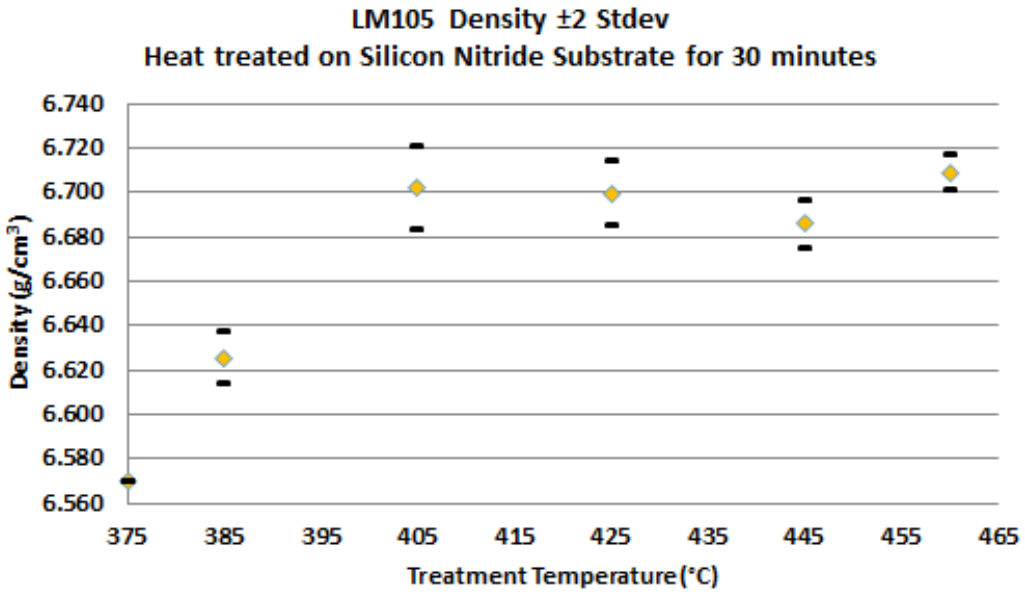

Figure 52. LM105 Density +-2 standard deviations when treated on silicon nitride substrate for 30 minutes.

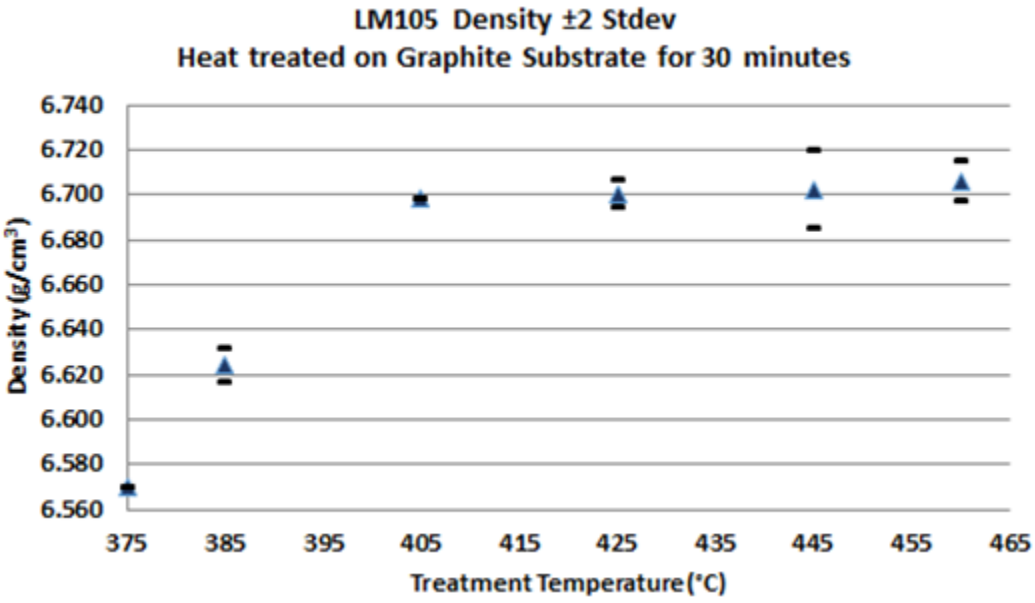

Figure 53. LM105 Density +-2 standard` deviations when treated on graphite substrate for 30 minutes.

E. SEM Surface Images

1. Zircon

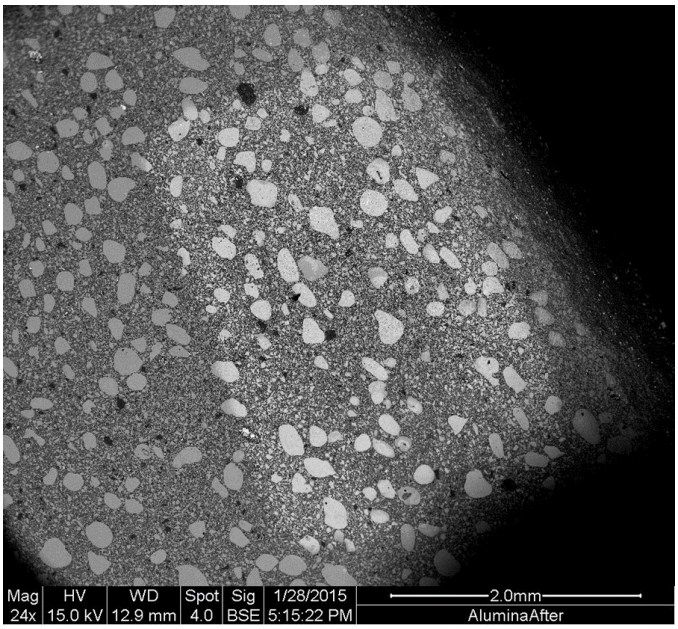

Figure 54. Backscatter image of zircon interaction region.

2. Alumina

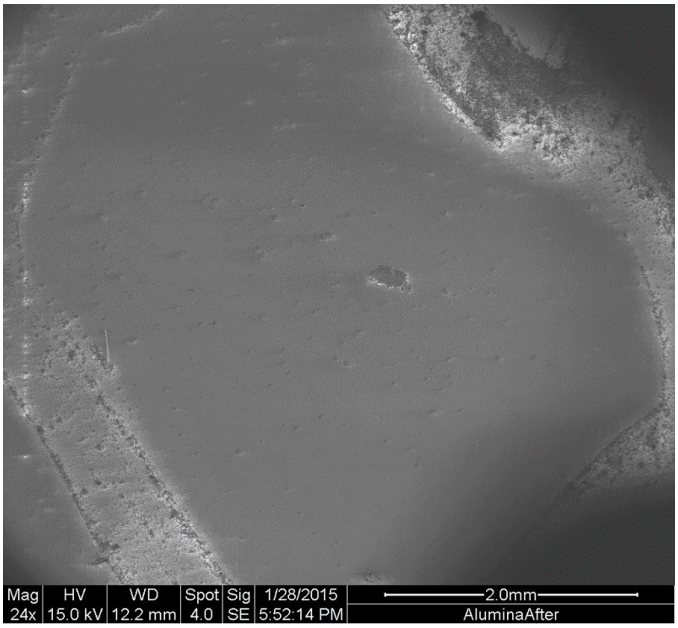

Figure 55. Scanning electron image of alumina after interaction.

3. Silicon Nitride

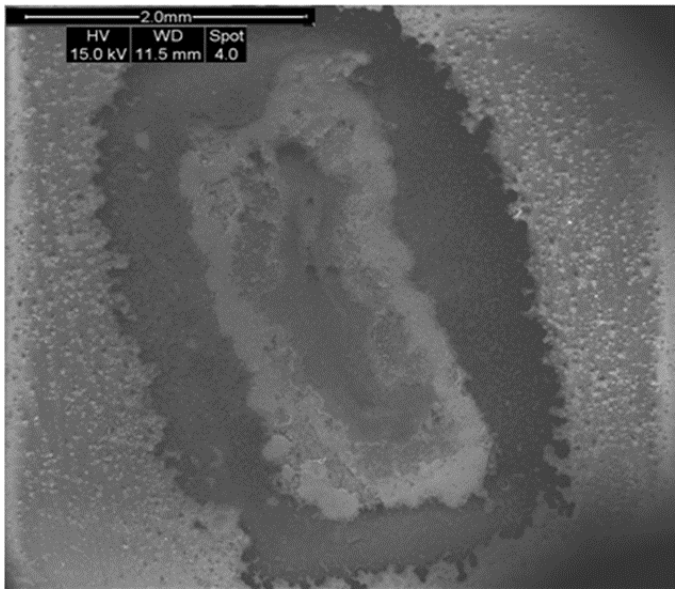

Figure 56. Scanning Electron image of silicon nitride interaction region.

4. Syalon 050

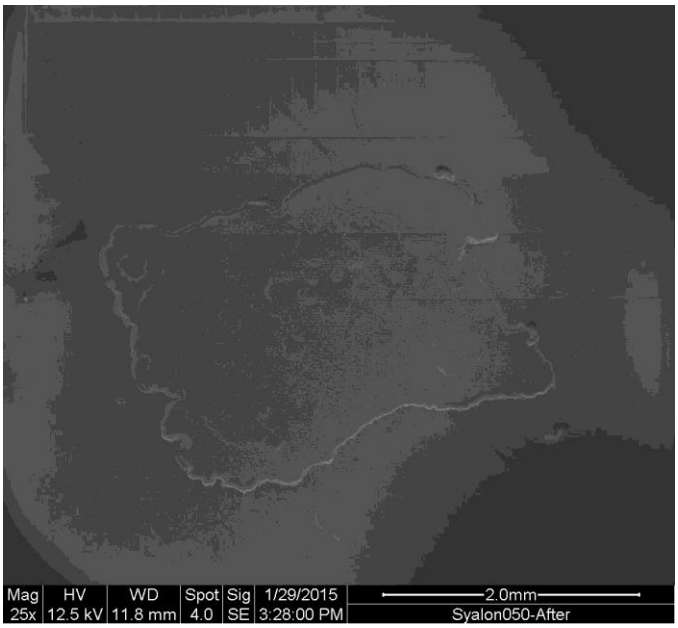

Figure 57. Scanning electron image of Syalon 050 after interaction.

5. Syalon 101

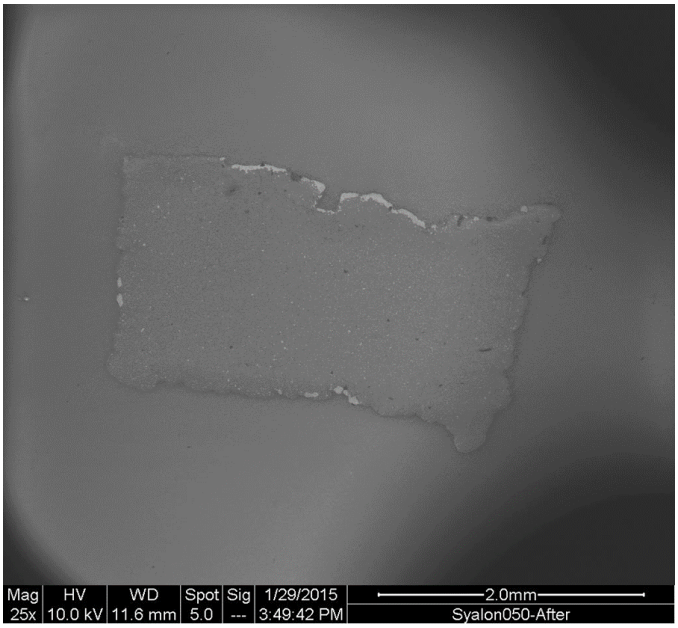

Figure 58. Combination backscatter and scanning electron image of Syalon 101 after interaction.

6. Syalon 110

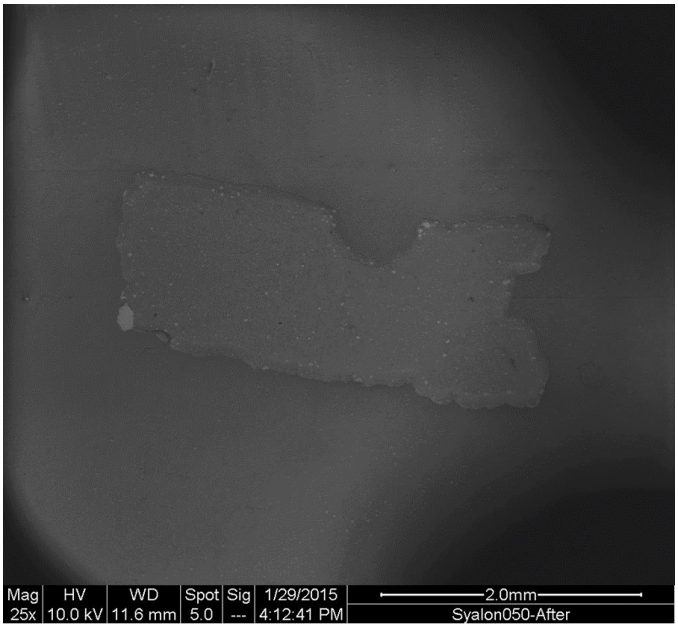

Figure 59. Combination backscatter and scanning electron image of Syalon 110 after interaction.

7. Syalon 201

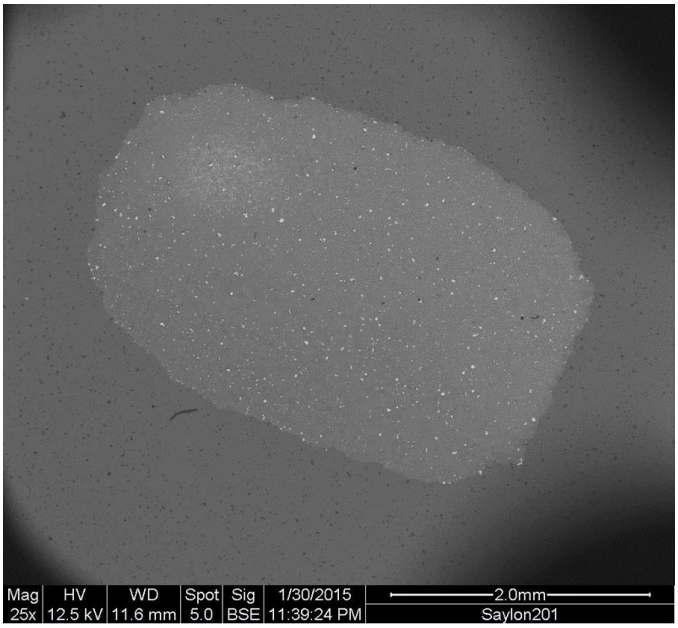

Figure 60. Scanning electron image of Syalon 201 after interaction.